

10

Velocimetry

In Chapter 9 we saw how diffusion tensor imaging, based on PGSE contrast, can be used to provide a localised map of average diffusion coefficients, diffusion anisotropy, and the orientation of the diffusion tensor principal axis frame. Similarly, the PGSE method can be used in combination with imaging methods for the purpose of velocimetry, the mapping of the local velocity field in a fluid sample.

Fluid motion can result in bulk movement of elements within sample, leading to changes in local (fluid) spin density, $\rho(\mathbf{r})$. NMR imaging can follow such changes provided that the image capture is rapid enough that spin positions do not significantly change during that process, and successive images can reveal slow changes in fluid density. Alternatively, if the motion is periodic, the image capture process can be stroboscopically gated to allow a faithful representation of cyclic motion.

However, in this chapter, as elsewhere in this book, we will be concerned with a sample for which the spin density remains constant with time, even though the spin-bearing molecules are in motion. That motion may be steady-state, with an associated Eulerian velocity field that is constant, or in fluctuation, in which case any imaging of velocity will need to be sufficiently rapid to capture these changes. There exist numerous methods for flow contrast that can give a simple and direct visualisation of motion and, as discussed in reference [1], may be broadly categorised as ‘steady state recovery’, ‘time of flight’, or ‘phase shift’ determinations. Steady state recovery methods rely on a rapid repetition of RF and gradient pulses such that the saturation recovery or steady state free precession signal amplitude depends on the spin motion. In time of flight methods, the appearance of an image is compared in real space at two different times, or a ‘bolus’ of spins is tagged at one time and imaged at some later time. Here we focus solely on developments, post reference [1], in ‘phase shift’ PGSE methods, and in particular their use in combination with MRI, so that the Eulerian velocity field, $\mathbf{v}(\mathbf{r})$, may be measured. Generally, such experiments can be labelled NMR velocimetry or, more specifically, when spatially resolved, as MRI velocimetry.

There are some underlying physical constraints with which all NMR velocimetry methods must contend [1], and these warrant re-statement. First, the range of average velocities that can be accurately determined will be limited by the receiver coil dimension, l , at the maximum, and by molecular self-diffusion at the minimum. To have an observable signal the moving spins must remain in the receiver coil over the observational timescale, of order the echo time TE over which displacements are tracked,

thus limiting velocities to less than or of order l/TE .¹ In non-imaging applications of flow measurement, where all spins within the coil are excited, there will always be a shift of spins located at the coil fringing field, and this effect will inevitably result in some signal degradation. In imaging, however, where slice selection is employed, such degradation can be avoided provided the excited spins remain within the receiver coil during image acquisition, although the slice selection gradient may itself introduce some additional velocity encoding.

The smallest average velocity that can be measured is limited simply by the superposed random motions of the molecules, although the degree to which random motion will mask the average flow is dependent on observational timescale. This is because flow displacements are linear with time, t , whereas rms diffusional displacements vary as $t^{1/2}$. The longest observational timescale, based on the use of stimulated echoes, is typically $t \sim T_1$. Thus the resolution of velocity measurements by NMR is of order $(D/T_1)^{1/2}$. For free water, this limit is around $50 \mu\text{m s}^{-1}$. For macromolecules or large particles with substantially smaller self-diffusion coefficients, even allowing for shorter T_1 values, this limit may well be below $1 \mu\text{m s}^{-1}$.

10.1 Imaging the propagator

Not long after the initial development of MRI techniques came the suggestion that bipolar (zero time integral) effective gradients could provide an image phase contrast proportional to velocity [5], and the imaging of mean flow rates by observing the dependence of pixel phase shifts on the first moment of $g^*(t)$ became well established [6, 7]. However, as we have seen earlier, the bipolar gradient pulse has the potential to provide a great deal more information than mean flow rates. In principle, it is possible to use narrow gradient pulse PGSE NMR to provide an average propagator for every pixel of the image, so that one is carrying out a measurement in both k - and q -space in the same experiment, a combination sometimes termed dynamic NMR imaging or dynamic NMR microscopy [8]. While costly in acquisition time, the combination of k -space and q -space imaging is a uniquely powerful method for determining local molecular ensemble behaviour in heterogeneous systems, providing in principle a resolution of order $10 \mu\text{m}$ for the static dimension, \mathbf{r} , and $0.1 \mu\text{m}$ for the dynamic dimension, \mathbf{R} .

10.1.1 Pulse sequence

The pulse sequence used for imaging the local propagator is essentially the same as that used for DTI. A spin warp version incorporating a single direction for q -encoding is shown in Fig. 10.1(a). With slice selection, imaging is performed in two dimensions, while the q -encoding represents the third dimension. In terms of total acquisition time, one k -dimension is a readout during acquisition, with the other a phase encoding requiring M separate acquisitions. M will typically be a multiple of 64, 128, or 256, depending on the spatial resolution and field of view required for the phase-encoding

¹Some ingenious experiments by Pines and co-workers [2–4] have demonstrated that spins borne by flowing molecules can be spatially encoded in one coil, but remotely detected downstream, thus extending the limits to timing resolution.

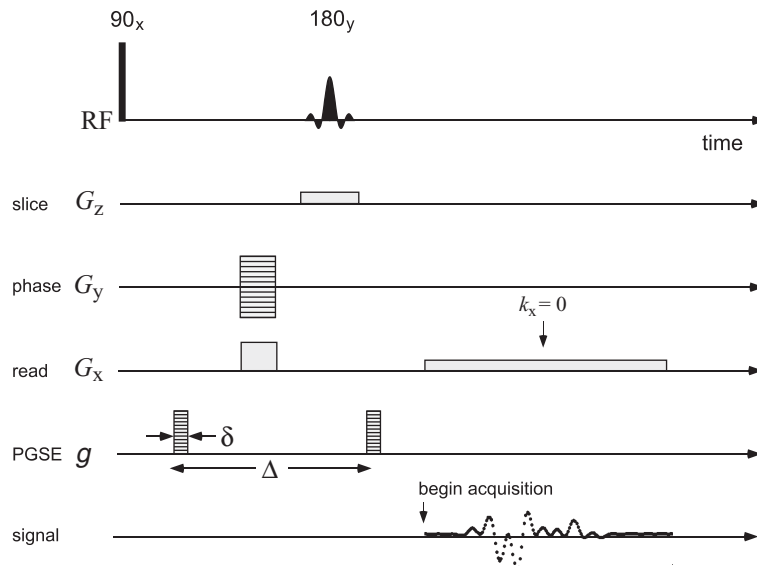


Fig. 10.1 Dynamic imaging pulse sequence incorporating both k - and q -space encoding. This particular spin warp imaging sequence, used in the experiments described in this chapter, employs a PGSE contrast period with, in this case, a spin echo. Long- Δ time interval experiments can be performed using a stimulated-echo version. Sampling of the echo as a function of k -space provides an image that has been further phase-encoded in q -space because of the PGSE gradients, which are stepped in amplitude between successive images.

dimension, the multiple being at least 2, for the most rudimentary ‘add–subtract’ phase cycle. Now include the q -steps, with the number again depending on the spatial resolution and field of view required for the displacement direction, and it is clear that on the order of 1000 or more signal acquisitions are needed.

10.1.2 Data processing

Data processing subsequent to the combined k - and q -encoding follows the flow chart illustrated in Fig. 10.2. First the inverse Fourier transform with respect to \mathbf{k} is carried out, for each separate q -encoded image, generating separate real and imaginary image sets. The method is therefore akin to a multi-slice experiment where successive slices are obtained in q -space rather than real space. Generally the total number, n_D of ‘ q -slices’ will be limited by the total available imaging time. However, a sufficient number of data points for accurate Fourier transformation, an analysis can be obtained by zero-filling the data, **provided that the signal has sufficiently attenuated by the n_D th slice.** One commonly encountered ensemble motion comprises a combination of mean flow and molecular self diffusion. A velocity and diffusion map for each pixel in an image can be obtained by computing the width and offset of the propagator in Z space. In practice the dynamic profiles are computed by stepping the PGSE gradient in n_D steps to some **maximum value g_m .** Given that the q -space interval is $\gamma\delta(g_m/n_D)$, the

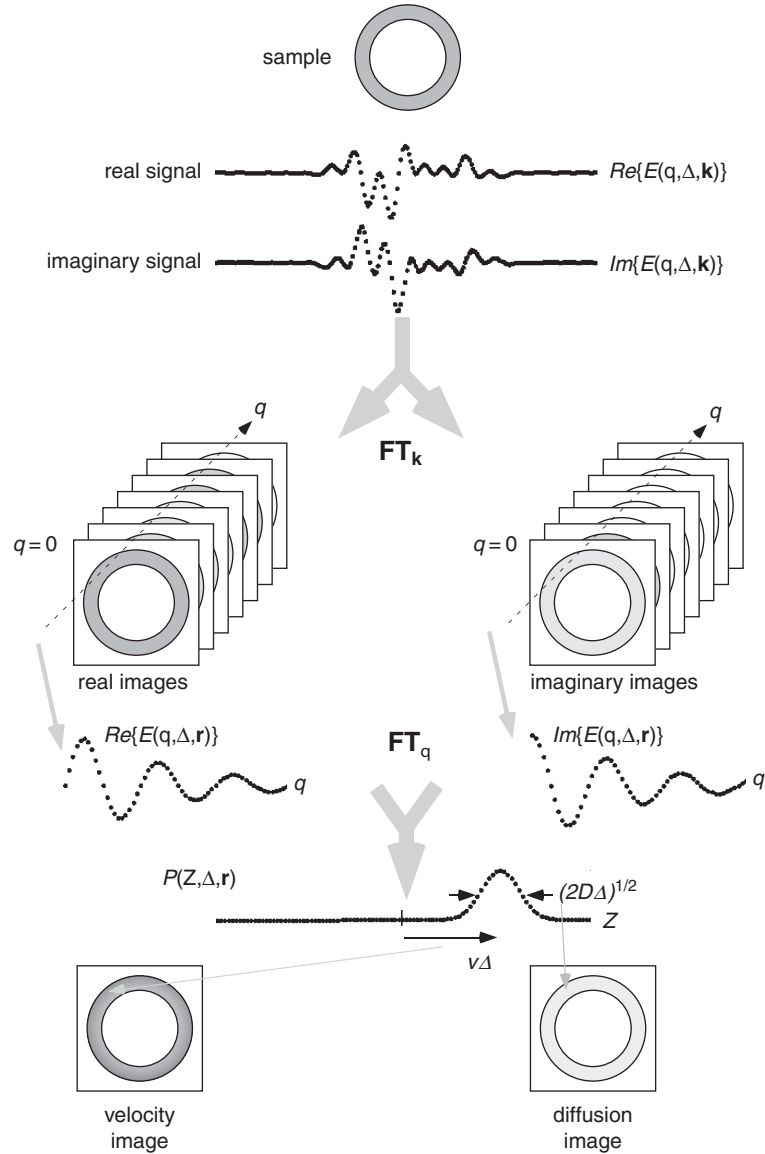


Fig. 10.2 Flow chart for processing in dynamic NMR microscopy.

complex signal, at pixel \mathbf{r} of the n th q slice following the k -space FT, has separate oscillatory and damping components arising from flow, v , and diffusion, D , as

$$\begin{aligned}
 E(q, \Delta, \mathbf{r}) &= E(0, \Delta, \mathbf{r}) \exp [iqv\Delta] \exp [-q^2 D\Delta] \\
 &= \rho(\mathbf{r}) \exp [i(\gamma\delta v\Delta)(g_m/n_D)n] \exp [-\gamma^2 \delta^2 (g_m/n_D)^2 D n^2 \Delta]
 \end{aligned} \tag{10.1}$$

where the density image is recovered for $q = 0$ so that $E(0, \Delta, \mathbf{r})$ may be rewritten as the local NMR image density, $\rho(\mathbf{r})$, corresponding to that pixel. By implication v and D will depend on the chosen pixel and are therefore functions of \mathbf{r} . Further Fourier transformation with respect to q along the n dimension results in a one-dimensional spectrum for each pixel,² corresponding to the dynamic displacement profile (averaged propagator) at \mathbf{r} .

Suppose that an N -point digital FT is performed, resulting in N displacement spectrum points between $\pm Z_{max}$, where the field of displacement is $2Z_{max} = (2\pi n_D)/(\gamma \delta g_m)$. Given the product shown in eqn 10.1, the propagator is the convolution

$$\bar{P}(k/N, \Delta) = (\pi n_D^2 / \gamma^2 \delta^2 g_m^2 D \Delta)^{1/2} \exp \left[-\pi^2 k^2 n_D^2 / \gamma^2 \delta^2 g_m^2 N^2 D \Delta \right] \\ \otimes \delta(k/N - \gamma \delta v \Delta g_m / 2\pi n_D) \quad (10.2)$$

where k is the digital value along the displacement direction and ranges between $-N/2$ and $N/2 - 1$. The peak centre occurs at the digital value

$$k_v = N \gamma \delta v \Delta g_m / 2\pi n_D \quad (10.3)$$

and so the value of the mean molecular velocity in the pixel corresponding to the profile is

$$v = 2\pi n_D k_v / N \gamma \delta v \Delta g_m \quad (10.4)$$

The full-width-half-maximum (FWHM) of \bar{P} in digital units is given by

$$k_{FWHM} = (2/\pi)[\ln(2)]^{1/2} N \gamma \delta(g_m/n_D)(D\Delta)^{1/2} \quad (10.5)$$

and the value of the mean molecular self-diffusion coefficient in the pixel corresponding to this profile is

$$D = (n_D k_{FWHM})^2 / [(4 \ln(2) / \pi^2) \gamma^2 \delta^2 g_m^2 N^2 \Delta] \\ = 3.56 (n_D k_{FWHM})^2 / [\gamma^2 \delta^2 g_m^2 N^2 \Delta] \quad (10.6)$$

The location of peak centre position, k_v , and peak FWHM, k_{FWHM} , can be achieved by a simple computer algorithm [9].

10.1.3 Velocity resolution limit

The lower limit to velocity resolution, gradient strength permitting, is determined by the competitive stochastic motion due to self-diffusion. The precision in the velocity measurement will be limited by the width of the Gaussian propagator, the standard deviation of which is $(2D\Delta)^{1/2}$, and, at first sight, one might assume that the error in the velocity is $\sqrt{2D}/\Delta$. However, in practice the determination is made by locating the peak of a distribution, a process the precision of which is limited by the rms noise in the propagator, δP . Taking the derivative of the propagator near its peak with

²Note that at this point, correct ‘phasing’ of the spectrum can be applied.

456 Velocimetry

respect to small deviations in velocity, δv , it is clear that the velocity determination error is given by [10]

$$\delta v = \sqrt{\frac{2D}{\Delta} \frac{\delta P}{P}} \quad (10.7)$$

where $\delta P/P$ is the noise-to-signal ratio in the propagator measurement. Clearly the best velocity resolution is achieved using the longest possible encoding time Δ , but at the same time the smallest flow displacement that can be measured results from using the smallest possible Δ consistent with the requirement that the random displacements due to self-diffusion do not dominate.

10.1.4 Velocity null experiments

With typical repetition times on the order of seconds, the pulse sequence of Fig. 10.1 implies a 30-min experiment at least, fine for steady-state flow, but of limited use when dealing with transient phenomena. Any speeding up requires trade-offs, and these are discussed in later sections. For the moment, we note that the fully multiplexed pulse sequence of Fig. 10.1 can be simply modified to allow for investigations of fluctuations, as shown in Fig. 10.3.

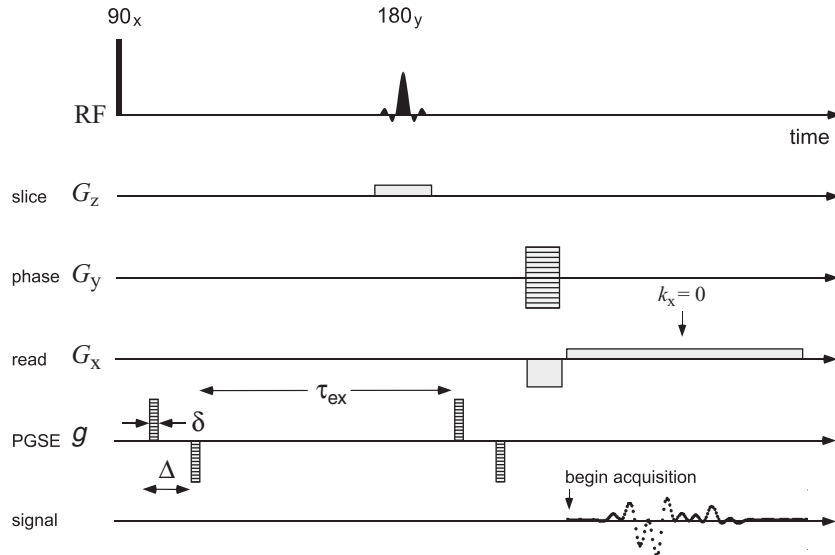


Fig. 10.3 Double PGSE version of the dynamic imaging pulse sequence of Fig. 10.1 used to investigate flow fluctuations.

By use of double PGSE encoding, a null displacement is returned where the dynamics are steady, the width of the average propagator being determined by self-diffusion alone. Any fluctuations over the time τ_{ex} between the PGSE pairs results in finite phase shifts, thus significantly broadening the propagator. The method does not directly visualise fluctuations, but it does detect their existence and their characteristic times. An example of this use is shown in Fig. 10.4, involving shear banded flow of

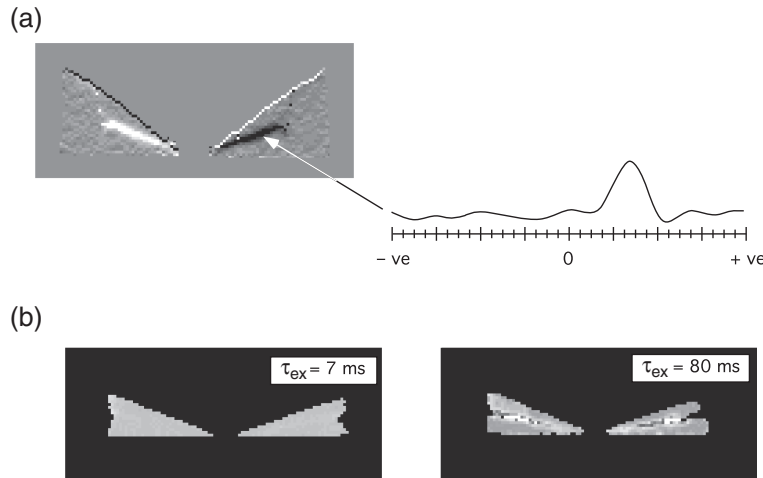


Fig. 10.4 (a) Velocity image for cetyl pyridinium chloride/sodium salicylate wormlike micelle solution in a 16-mm diameter 7-degree cone-and-plate system with a $\times 6$ vertical gain (pixel size $156 \mu\text{m} \times 26 \mu\text{m}$), at an apparent shear rate of 10.7 s^{-1} . Note the shear band indicative of a lower viscosity fluid state, near the centre of the gap. The average propagator shown is taken from a pixel inside the shear band, as indicated. (b) FWHM image for solution (a) at an apparent shear rate of 14.3 s^{-1} in the 25 mm, 7-degree cone-and-plate system with $\times 3$ vertical gain, obtained using the double PGSE pulse sequence with exchange times of 7 ms and 80 ms. (Adapted from reference [11].)

wormlike micelles in a cone-and-plate geometry.³ Figure 10.4(a) shows the gap of the 7-degree cone-and-plate cell with the vertical (y) gain expanded by a factor of 6. The grey scale intensity is a measure of the local shear rate $\partial v_z / \partial y$, where z is the flow direction normal to the page. A band of high shear rate is visible at gap centre, a consequence of the micellar solution undergoing a non-equilibrium phase transition to co-existing states of differing viscosity. A sample propagator is shown taken from a pixel within the low viscosity shear band.

Figure 10.4(a) is the result of a double PGSE encoding experiment at two different exchange times of 7 ms and 80 ms [11]. Here the grey scale plots the FWHM of the propagator. At $\tau_{ex} = 7 \text{ ms}$ the FWHM is common to all pixels in the image, irrespective of proximity to any shear band, while at 80 ms, a distinct FWHM enhancement results, thus revealing the existence of banding fluctuations at intermediate timescale.

10.2 Single-step phase encoding for velocity

Imaging the complete propagator comes at the price of multiple encoding steps in q -space. While the consequent commitment of imaging time provides valuable information concerning details of the molecular translational dynamics in each pixel, where all we seek is the mean local flow rate, a simpler, more time-efficient procedure is to

³See Section 10.4.3.

use a single q step. Of course, the more values of q we use, the more precisely we can determine the local velocity, but if we are prepared to trade away some of this precision, on the understanding that our intrinsic image signal-to-noise ratio is sufficient, then the combination of a reference $q = 0$ image and a finite q image allows for a velocity map to be generated.

10.2.1 Reference phase processing

Consider a particular pixel of two corresponding images obtained with $q = 0$ and $q = q_1$. The resulting complex signals are $E(0, \Delta, \mathbf{r})$ and $E(q_1, \Delta, \mathbf{r})$. If the mean flow in that pixel is v , then we may write

$$\frac{E(q_1, \Delta, \mathbf{r})}{E(0, \Delta, \mathbf{r})} = A \exp(i\phi) \quad (10.8)$$

where $\phi = q_1 v \Delta$ and $A \lesssim 1$ is the attenuation factor due to diffusive effects. The phase angle ϕ may be directly calculated from the complex number represented by eqn 10.8, for example using the Matlab function reference, ‘angle’.

For any sensible experiment, we will require that the diffusive attenuation be not so great that the signal-to-noise ratio of the finite q image is significantly deteriorated beyond that of the $q = 0$ image. In other words, if f_σ is the fractional rms noise in each pixel, then we require $f_\sigma \ll A$.

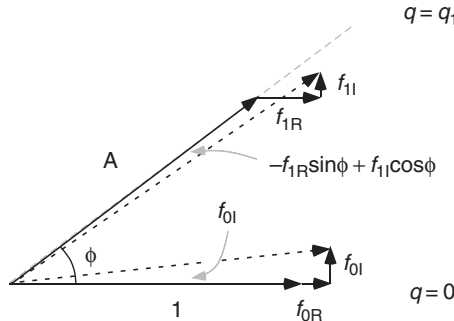


Fig. 10.5 Argand plane representation of $q = 0$ and $q = q_1$ signals for a particular image pixel, showing the influence of noise. $A \lesssim 1$ is the attenuation factor due to diffusive effects, where we require $A \gg f_\sigma$, f_σ being the rms value of the real and imaginary noise contributions.

Let us write the complex fractional noise in the cases $q = 0$ and $q = q_1$ for the pixel at \mathbf{r} as $f_{0R} + i f_{0I}$, and $f_{1R} + i f_{1I}$, respectively, each noise term having the same rms value f_σ . Reference to Fig. 10.5 shows that the resulting error in the determination of the angle ϕ is

$$\delta\phi = -f_{0I} - f_{1R} \sin \phi + f_{1I} \cos \phi \quad (10.9)$$

By summing the noise power $f_{0I}^2 + f_{1R}^2 \sin^2 \phi + f_{1I}^2 \cos^2 \phi$, we see that the rms error in the angle determination is

$$\langle (\delta\phi)^2 \rangle^{1/2} = \sqrt{2} f_\sigma \quad (10.10)$$

Calculating the mean flow by finding the argument of the ratio $E(q_1, \Delta, \mathbf{r})/E(0, \Delta, \mathbf{r})$ represents a quick and efficient data-processing scheme. An alternative is to use a Fourier analysis akin to that applied for multi- q experiments as shown in Fig. 10.2. In the next section, we show that these approaches are practically equivalent.

10.2.2 Fourier analysis

Having obtained $q = 0$ and $q = q_1$ images, we can generate a multi- q data set by adding zero-filled images. Suppose we make an N image set. Fourier transforming with respect to q will generate an average propagator for each pixel, but the dominant broadening for that propagator will arise not from diffusion, but from the effect of truncation at the second q step. In effect, the propagator is a convolution of the ideal propagator with a sinc function, the spectrum of the step function that truncates the data set. Labelling the digital steps in the q -domain by $0 < n < N - 1$ and in the propagator-domain by $-N/2 < k < N/2 - 1$, and using the definition of the digital Fourier transform given in eqn 4.44, we have the propagator given by

$$P\left(\frac{k}{N}\right) = 1 + \exp(i2\pi\frac{k}{N} - i\phi) \quad (10.11)$$

An example of this function, for $N = 128$ and $\phi = 0.2$ radians, is shown in Fig. 10.6. Our task is to find the k -coordinate of the maximum of this function, enabling us to directly determine ϕ . In the absence of noise, $\phi = 2\pi k_v/N$. Noise introduces uncertainty $\delta\phi$.

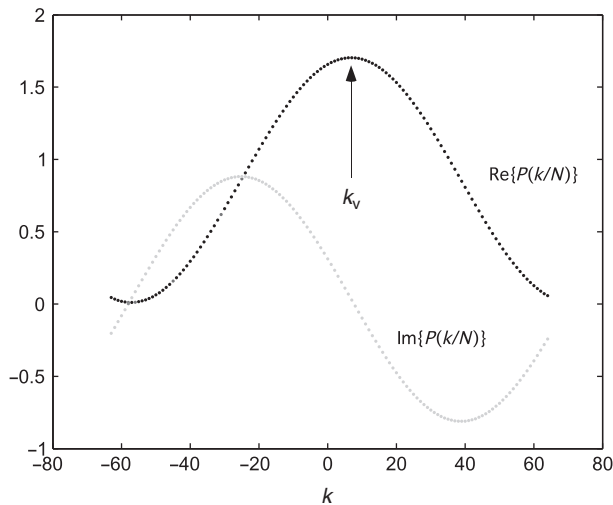


Fig. 10.6 Apparent propagator generated from Fourier transformation of a truncated q -space in which only $q = 0$ and $q = q_1$ steps are used. The real part of the phased propagator has a maximum at $k_v = N\phi/2\pi$. In this example $\phi = 0.2$ radians and $N = 128$.

Now we include the role of noise. The real and imaginary parts of eqn 10.11 become

$$\begin{aligned} \text{Re}\{P\left(\frac{k}{N}\right)\} &= 1 + \cos(2\pi\frac{k}{N} - \phi) + f_{0R} + f_{1R} \cos(2\pi\frac{k}{N}) - f_{1I} \sin(2\pi\frac{k}{N}) \\ \text{Im}\{P\left(\frac{k}{N}\right)\} &= -\sin(2\pi\frac{k}{N} - \phi) + f_{0I} + f_{1I} \cos(2\pi\frac{k}{N}) + f_{1R} \sin(2\pi\frac{k}{N}) \end{aligned} \quad (10.12)$$

In fact, eqn 10.12 represents the correctly phased propagator. The unknown absolute phase of the NMR signal is unimportant when we calculate the flow-induced phase shift by taking the ratio in eqn 10.8. However, in using the Fourier method an additional autophasing step is needed. Here we assess the separate contributions to $\delta\phi$ from the maximum finding and autophasing procedures.

why autophasing ??

In autophasing, an arbitrary phase angle θ is adjusted in a multiplicative term, $\exp(i\theta)$, until the integral of the real part of $P\left(\frac{k}{N}\right)$ is maximised, or until the integral of the imaginary part of $P\left(\frac{k}{N}\right)$ is zero. Any error in θ due to the effect of noise becomes an error in ϕ . Since the integral of the f_{1I} and f_{1R} noise terms in eqn 10.12 are necessarily zero, the noise contribution to an error in the integral of $\text{Im}\{P\left(\frac{k}{N}\right)\}$ is iNf_{0I} . The discrepancy in the signal integral between the correct phase θ and the shifted phase $\theta + \delta\phi$ is $N[\exp(i\delta\phi) - 1] \approx iN\delta\phi$. Whence, for autophasing, $\delta\phi = f_{0I}$.

how to do autophasing

not quite understand

In finding the maximum of $\text{Re}\{P\left(\frac{k}{N}\right)\}$ the signal shape is unaffected by the constant noise term f_{0R} , but distorted by the sinusoidal variation of $f_{1R} \cos(2\pi\frac{k}{N}) - f_{1I} \sin(2\pi\frac{k}{N})$ in the vicinity of the maximum, $2\pi n/N = \phi$. Given a positional discrepancy of $\delta\phi$, the problem reduces to finding the null in the derivative of $\text{Re}\{P\left(\frac{k}{N}\right)\}$, i.e. the function $\sin(\delta\phi) + f_{1R} \sin(\phi + \delta\phi) + f_{1I} \cos(\phi + \delta\phi)$. The small signal null offset, $\sin \delta\phi$, is counterbalanced by the local noise term contribution to the slope, to first order, $f_{1R} \sin \phi + f_{1I} \cos \phi$. Thus we have, for maximum finding,

$$\delta\phi = f_{1R} \sin \phi + f_{1I} \cos \phi \quad (10.13)$$

Combining the autophasing and peak finding errors, we end up with a total error $\langle(\delta\phi)^2\rangle = \sqrt{2}f_\sigma$, independent of the number of points, N , used in the zero filling, and identical to that given in eqn 10.10 for the ratio method of phase determination.

10.2.3 Choice of method

Having established the equivalence of the ratio and Fourier spectrum methods in the case of a single phase-encoding q step, it is worth pointing out that both methods allow easy inclusion of extra phase-encoding steps, with consequent gains in the precision of velocity determination. Again, both appear equivalent in their precision, but perhaps the advantage of the Fourier method being an asymptotic behaviour towards an accurate representation of the pixel propagator as the number of q steps is increased sufficiently to significantly attenuate the image.

The result $\langle(\delta\phi)^2\rangle = \sqrt{2}f_\sigma$ means that some care is needed in experimental design. For example, a signal-to-noise ratio in each pixel of 10:1, a good result in any imaging experiment, implies that angular precision is on the order of 0.1 radians. The essential requirement in single-step phase-encoding is the need to ensure that the magnitude of

q_1 is large enough to give a phase shift significantly larger than the fractional signal-to-noise ratio.

Finally, it is worth noting that single-step encoding requires only one reference image at $q = 0$. Subsequent measurements need only single q_1 images to monitor a changing velocity field. Therein lies its real power.

10.3 Fast encoding and real-time velocimetry

The use of single-step phase encoding for flow certainly reduces the ‘frame rate’ at which a transient velocity field may be monitored. In this section are outlined some general principles concerning velocimetry speed. First we must clearly understand two questions. What are the characteristic times associated with the velocimetry pulse sequence? What are the characteristic times associated with the flow? So prepared, we are in a position to understand how these timescales intersect.

10.3.1 Flow timescale

The most important subdivision of fluid flow is between steady-state and transient. Steady-state refers to the time-independence of the Eulerian flow field, $\mathbf{v}(\mathbf{r})$. In transient flow, this field acquires a time dependence, $\mathbf{v}(\mathbf{r}, t)$. But NMR is essentially a Lagrangian flow method, in which the signal is derived from spins co-moving with the fluid. These velocities may vary with time, even under steady-state flow, as spins migrate to different positions in the flow field. And when we encode for position, as in MRI, the spatial coordinates acquired derive from the location of those spins at the time of that encoding.

Perhaps the best way to visualise the problem is by way of simple examples, as shown in Fig. 10.7. Here we see, in (a), (b), and (c), three examples of steady-state flow, namely laminar pipe flow, laminar converging flow, and laminar cylindrical Couette flow. Example (f) shows the flow within a falling droplet driven by surface stress due to a surrounding viscous fluid. Again the flow is steady state within the droplet, though stroboscopic methods might be needed to ‘lock’ the droplet frame to the velocimetry frame. Any periodic flow falls into the same category as example (f). By contrast, in examples (d) and (e), showing, respectively, trickle bed flow under fluctuating conditions and turbulent flow, we see the Eulerian flow field changing, with perhaps a characteristic time τ_c .

10.3.2 Velocimetry timescale

There are three timescales associated with velocimetry. These are the phase-encode time for velocity, Δ , the time to acquire the spatial locations of the spins, τ_{MRI} , and the image-refresh time, τ_R .

Δ is never a limiting timescale for fast flows. To ascertain the mean flow rate in an image pixel, we need only allow for a displacement that overwhelms the broadening due to diffusion. For convenience we may take the example of water molecules, where the diffusion length over 1 ms is on the order of a few microns. Flow rates of $\gtrsim 1 \text{ m s}^{-1}$ can be captured in 1 ms. Slower rates take accordingly longer.

Now to position capture: in a 1-D spatial imaging experiment with single-step phase-encoding for velocity, and a readout gradient for position, $\tau_{MRI} = \tau_{read}$ can be

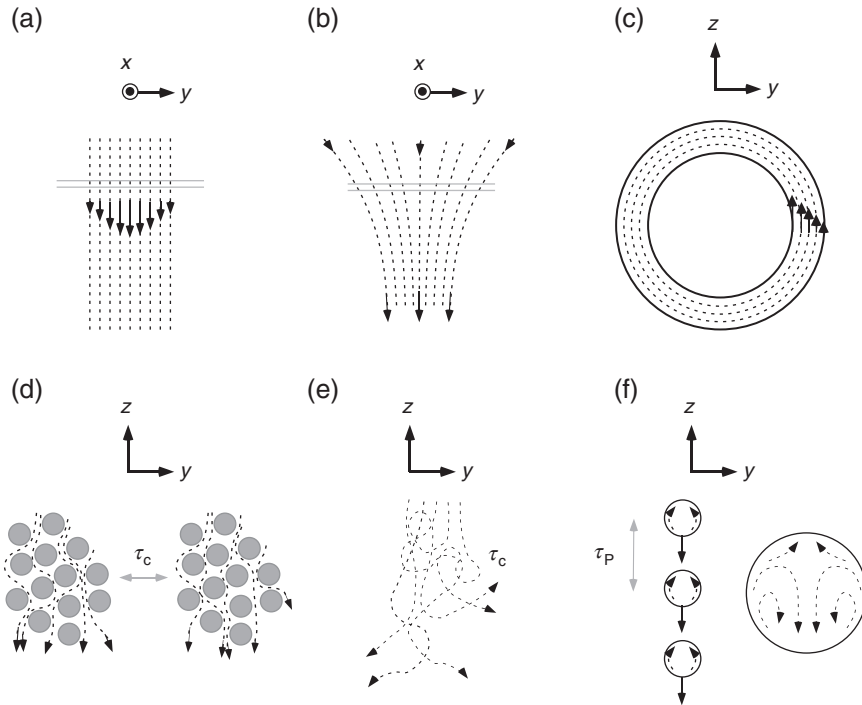


Fig. 10.7 Schematic representation of different flows in which characteristic times play a role. In each case a 2-D image acquisition is assumed and the imaging plane indicated by the axes. (a) Steady-state laminar pipe flow. (b) Laminar converging flow. (c) Laminar cylindrical Couette flow. (d) Trickle bed flow under fluctuating conditions. (e) Turbulent flow. (f) Periodic flow with stroboscopic imaging of a falling droplet.

as short as a few milliseconds. The refresh interval will be the sum of Δ , τ_{read} , and any recovery time associated with spin relaxation. In some fortunate circumstances, for example where the velocity being measured is predominantly normal to the imaging strip in a 1-D image, the flow itself brings fresh spins to the image so that relaxation delays are no longer limiting. Alternatively, and provided one is prepared to pay the consequent signal-to-noise ratio price, small tip-angle excitation pulses may be used to allow further longitudinal magnetisation recall. In short, 1-D velocimetry is well suited to rapid flows, with potential refresh times on the order of a few milliseconds. The real challenge comes with 2-D or 3-D imaging of flow fields. However, as we shall see, for steady-state flow, the problem vanishes.

2-D and 3-D MRI images may be acquired in spin-warp mode by using readout (frequency encoding) for one dimension and phase encoding for the remaining dimensions. Thus the basic sub-unit of the imaging sequence comprises the repetitive ‘excitation pulse and collect’ acquisition under readout gradient, allowing a repeat interval determined by T_1 recovery alone, perhaps in the range 0.1 s to 1 s, during which the phase gradients are stepped to their next value. The total image may take minutes to

acquire, but if the Eulerian velocity field is steady state, the only characteristic imaging times relevant to any artifact in determining the velocity field are the times Δ and the readout time, τ_{read} . For distortion-free imaging, we will require that the sum of these not exceed the time to move across one pixel in the 2-D or 3-D frame. Examples (b) and (c) in Fig. 10.7 are instructive in this regard. Here we have components of flow velocity ‘within the imaging plane’. As a simple exercise, for pixel dimensions of $50\ \mu\text{m}$ and Δ and τ_{read} on the order of milliseconds, speeds of tens of metres per second are easily manageable. The same ‘steady-state robustness’ is available with repetitive flows, such as the falling droplet example of (f), providing the ‘excitation pulse and collect’ is stroboscopically locked to the repetitive phenomenon.

As a result, the real timescale challenge for MRI velocimetry in 2-D or 3-D concerns fluctuating flows. If we are to capture the essentials of the flow timescale, we must complete the entire velocity and position encoding with a total refresh time τ_R shorter than any flow correlation time τ_c .⁴ The key to a rapid refresh rate is the ability to capture a 2-D image in the time interval associated with a single cycle involving a initial excitation RF pulse and the use of the consequent transverse magnetisation over a single relaxation interval. Three methods stand out, in order of decreasing speed and increasing robustness to image artifact. These are ‘echo planar imaging’ (EPI), ‘rapid acquisition relaxation enhanced imaging’ (RARE), and ‘fast low angle shot imaging’ or FLASH. Each of these is discussed in succession. Finally, we describe a slower, but highly robust velocimetry method based on pure phase encoding, known as ‘single-point ramped imaging with T_1 -enhancement’ or SPRITE.

[What is this](#)

10.3.3 Echo planar imaging

The fastest possible velocimetry technique uses the EPI scheme, the fast imaging method proposed and demonstrated by Mansfield and co-workers [12–15]. Following a slice excitation, k -space is sampled in two dimensions using a sequence of readout gradients applied in opposite directions, so that, by means of ‘blips’ of intervening phase gradient pulses advancing along the orthogonal axis one line at a time, a Cartesian plane is mapped out. These gradients can be seen in the repeat elements of the repeated EPI scheme shown in Fig. 10.8. Because multiple gradient echoes are used in the 2-D sweep, rather than employing a multiple spin-echo sequence to subdivide the successive readouts, EPI minimises the number of RF pulses needed, allows the greatest time compression in the spatial encoding, and avoids the defocusing of PGSE-encoded spin phases associated with multiple RF pulse trains, a subtle point to which we shall return in the next section when discussing RARE.

However, EPI suffers two particular drawbacks. Because it relies on gradient rather than spin echoes, it does suffer from dephasing, and hence image distortion, caused by background-field inhomogeneity. This need not be a limiting factor provided that the readout gradients are much larger than those contributed by the sample. The second problem with EPI concerns the fundamental asymmetry inherent in the opposite direction readout sweeps, unproblematic in an ideal implementation, but leading in practice to slightly inequivalent acquisitions on negative and positive gradient pulses,

⁴Note, however, the trick outlined in Section 10.1.4, in which a velocity-null experiment can be used to reveal fluctuations on order of Δ .

and hence a k -space modulation that can lead to severe image distortion and ‘ghosting’ effects. Exquisite care is needed in the implementation of EPI to minimise such artifacts and proper setup requires considerable skill.

The first use of PGSE-encoded EPI for rapid velocimetry was by Kose [16–18], although other researchers have reported the use of standard EPI-based techniques to investigate fluid flow from its influence on signal intensities in the image [19].

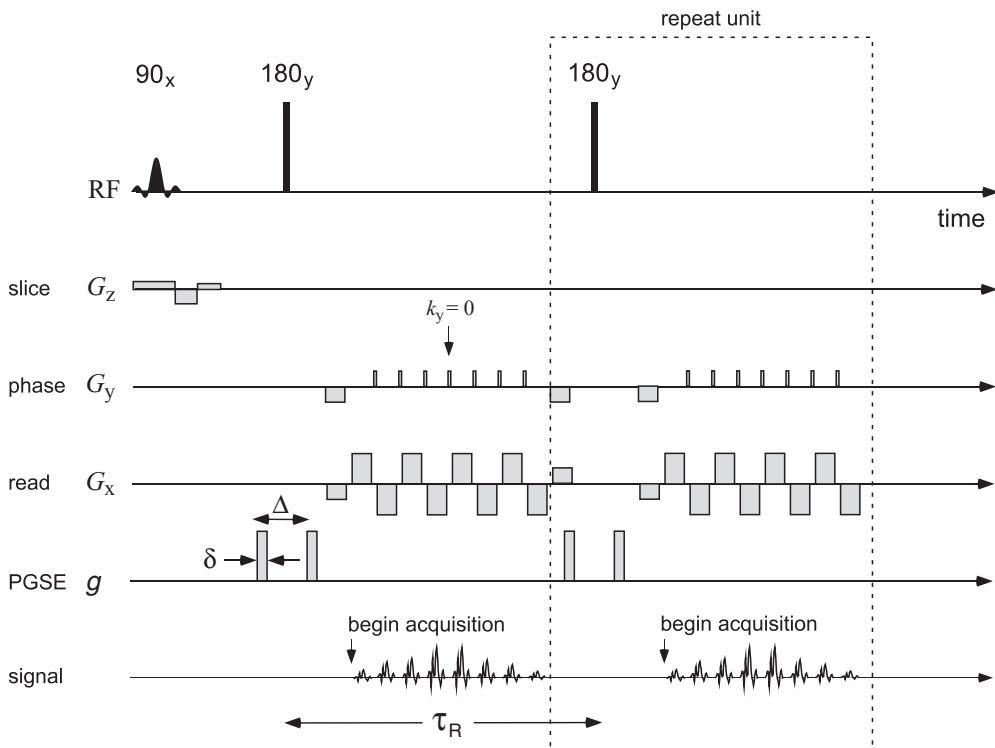


Fig. 10.8 GERVAIS version of a multiple EPI imaging sequence in which independent PGSE phase encoding for motion is performed in each successive repeat, thus allowing for rapid frame rate investigation of velocity fields, with a refresh time of τ_R .

However, the most comprehensive and powerful implementation of PGSE-encoded EPI is due to Sederman *et al.*, in a variant shown in Fig. 10.8, quixotically named GERVAIS for gradient echo rapid velocity and acceleration imaging sequence [20]. This group have been highly successful in implementing this EPI velocimetry method, achieving total image acquisition time as short as 10 ms, a repeat time τ_R of 20 ms, and a complete recycle time (duration to next slice excitation) of around 500 ms. Note the use of flow-compensated slice excitation, the positioning of that slice being made near the inlet end of the sensitive region within the RF coil, so to minimise outflow effects.

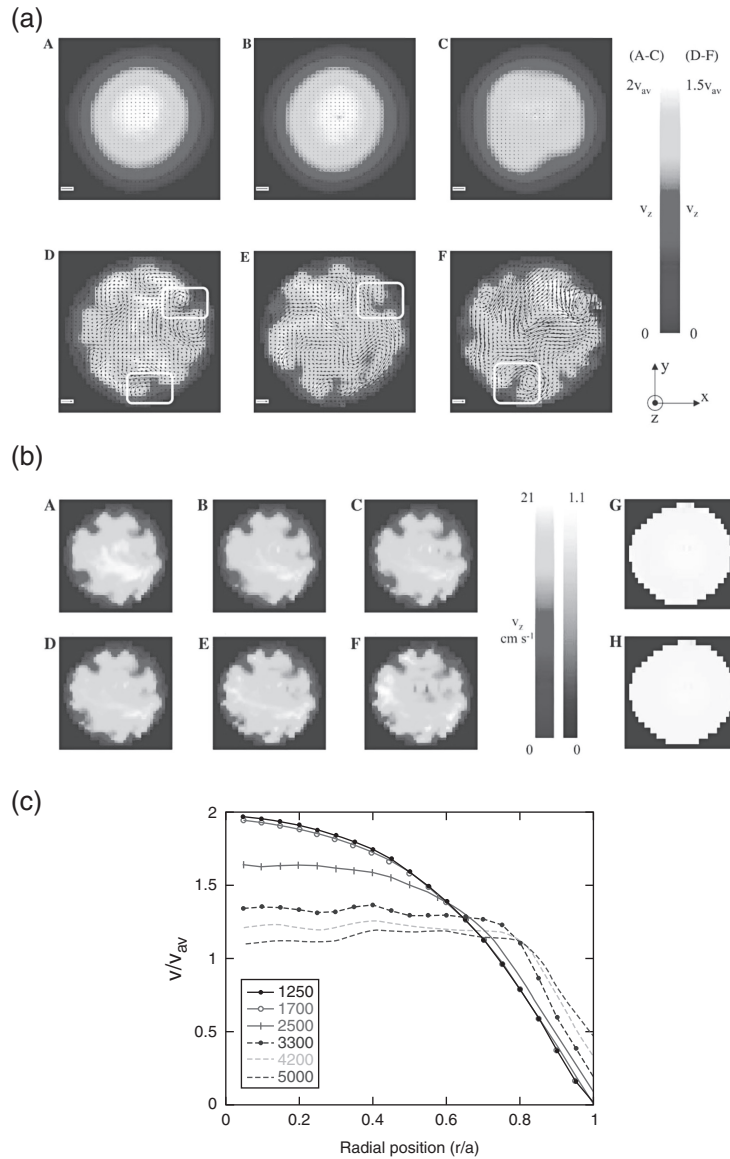


Fig. 10.9 (a) Three orthogonal component velocity images acquired at increasing Re of (A) 1250, (B) 1700, (C) 2500, (D) 3300, (E) 4200, and (F) 5000. The colour scale identifies the magnitude of the z -velocity. The flow velocity in the $x-y$ plane of the image is shown by the vectors. The vector scale bar on each image corresponds to 1 cm s^{-1} . (b) Six consecutive z -velocity images acquired at 20 ms time intervals are shown (A–F) for flow at $Re = 5000$. The average VACF maps calculated from pairs of images separated by time intervals of (G) 40 ms and (H) 80 ms are also shown. (c) Radial velocity profile of the z -velocity for Re in the range 1250–5000. (Reproduced with permission from Sederman *et al* [20].) This figure is reproduced in colour in the colour plate section.

Figure 10.9 shows a remarkable application of this rapid velocimetry technique in a study of the transition to turbulence for water in pipe flow as the Reynold's number is increased from 1000 to 5000. Figure 10.9(a) shows sets of images obtained over a 60 ms period, in which the flow-encoding gradient q is successively switched between the x , y , and z directions in successive 20 ms repeat intervals. With increasing Re a transition to turbulence is seen, in which significant transverse velocity components emerge. By tracking the longitudinal velocity at 20 ms intervals, a picture emerges regarding the characteristic fluctuation rate, from which a velocity autocorrelation function map can be calculated. Finally the v_z flow profile shows the classic transition from Poiseuille flow to plug flow as the turbulent regime is entered.

10.3.4 Rapid acquisition relaxation enhanced imaging

While RARE cannot match EPI for speed, it has the significant advantage of image robustness. The reason for this is its resilience to instrumental errors, due to the fundamental symmetry of the k -space sampling scheme, along with resilience to sample susceptibility heterogeneity by the use of a multiple spin-echo train, which refocuses unwanted phase shifts caused by background field gradients. In a pure RARE imaging experiment, the matter of symmetry under a CPMG RF pulse train is dealt with nicely. This can be seen by reference to the RARE part of the velocimetry sequence shown in Fig. 10.10. Each echo acquisition under the read gradient involves a single traverse (from left to right) across the k_x axis of the Cartesian grid. The precursor phase gradient has swept the spins to start the k -space traverse along a particular k_x line positioned as desired on the orthogonal k_y axis, but at the end of the sweep an unwind phase gradient returns the signal to $k_y = 0$. Thus, at the start of every echo interval, the spins are identically positioned in k -space.

However, as we shall see, when RARE is combined with a precursor PGSE gradient pulse pair to encode for motion, the CPMG RF pulse train introduces a new problem, namely the ability of multiple imperfect 180° pulses to preserve the in-phase component of magnetisation, while permitting phase decoherence to occur for the out of phase component. This problem needs to be specifically addressed with PGSE-RARE.

Sederman *et al.* [21] investigated pipe flow at 40 mm s⁻¹ using a RARE sequence without PGSE encoding, while Scheenen *et al.* combined RARE with both PGSE and spin-echo encoding [22, 23] to study the water uptake in plant stems, e.g. liquids under very small flow rates (~ 0.5 mm s⁻¹). A modified version [24] of the PGSE-encoded RARE pulse sequence of Scheenen *et al.* is shown in Fig. 10.10. Here we look in detail at the way in which flow introduces new artifacts, and how these may be suitably countered in the pulse sequence design.

Soft-pulse-quadrature-cycled PGSE-RARE

The use of hard 180° RF pulses in the RARE part of the imaging sequence can lead to significant artifacts in which a part of the intensity in the central part of the image, where flow occurs, is transferred to the image border, the so-called 'ghosting' associated with ± signal modulation with respect to the successive phase steps. Such an amplitude alternation leads, by the shift theorem, to a 'ghost' image displaced by half the field of view. The intensity of this artifact depends on the velocity-encoding

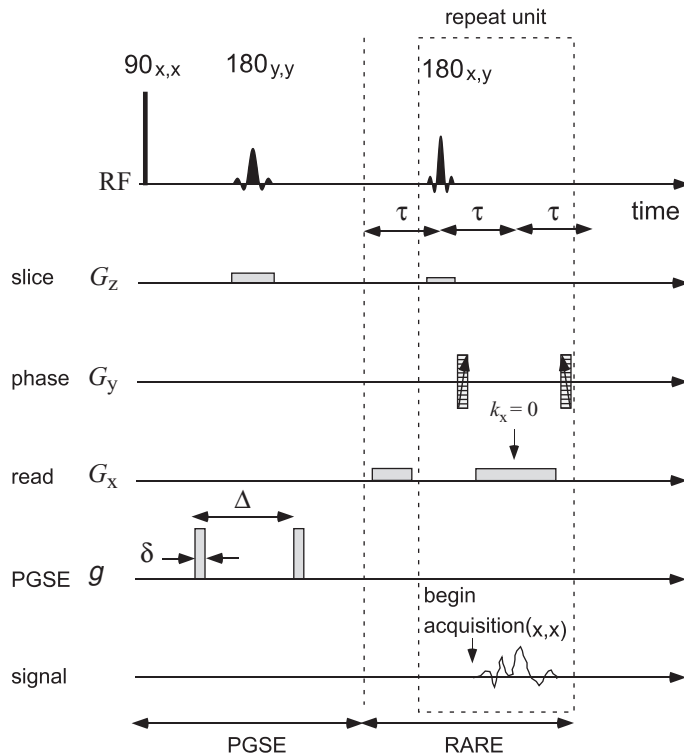


Fig. 10.10 Velocimetry pulse sequence based on RARE using soft pulses within the CPMG train. Note the use of shorter, more intense soft pulses in conjunction with a smaller slice gradient in the train to excite a large sample volume, but within the homogeneous region of the RF coil. The phase-encoding scheme involves wind and unwind pulses sandwiching each echo acquisition, so that the signal is return to the k_y (phase direction) origin before the next 180° RF pulse.

gradient strength applied, as well as on the velocity of the fluid itself. In other words, while these artifacts are a consequence of the imaging process, adding flow and q -gradients enhances them. The explanation is obvious and as old as the original paper by Carr and Purcell [25], who noted that odd and even echoes alternate in amplitude due to RF pulse imperfections, while flow induces even more severe odd-even alternation. ‘Ghosting’ artifacts can be mostly eliminated by the use of only the even echoes within the RARE part of the pulse sequence, the price paid being a doubled pulse sequence duration. Further, replacing the hard pulses in the CPMG train by soft pulses with the slice gradient chosen to include only spins within the uniform RF field region of the resonator causes a significant reduction in ghosting artifacts.

The second RARE artifact associated with PGSE phase encoding concerns the loss of the imaginary part of the NMR signal during the multi 180° RF pulse segment of the pulse sequence, a general feature of sequences based on the CPMG sequence [25]. This problem is not necessarily fatal, but is certainly inconvenient. The loss of the imaginary

signal leads to a symmetrical positive and negative flow mirroring of the propagator in the subsequent Fourier transformation of the acquired data with respect to the q direction, as the input data are no longer modulated by an exponential function with a complex argument but instead experience a cosine modulation. While such mirroring may be acceptable at large propagator displacements, at low velocities it leads to overlap distortions. Further, with single q -step encoding, the mirroring effect is highly undesirable, since it impedes a proper phase angle calculation and renders the truncated propagator ambiguous.

The means by which this effect may be overcome is seen in the variant known as soft-pulse-quadrature-cycled PGSE-RARE [24], shown in Fig. 10.10. To avoid the cosine modulation effect and restore the full complex signal, one needs a two-step phase cycle in which the excitation phases are identical, while the phase of the 180° pulse train switches between x and y in two separate RARE acquisition trains, so that real and imaginary magnetisation is independently protected and stored. Thus the whole complex NMR signal is accumulated in the acquisition memory. One might expect that the acquisition phase should alternate between x and $-x$ because of the changing sign of the echo under 180_y and 180_x RF pulses, though in practice a fixed acquisition phase works equally well. The reason is that the ‘non-protected’ component dies away rapidly along the CPMG train and contributes little to the image, resulting in separate storage of real and imaginary signals in the two separate parts of the phase cycle. Hence (x, x) or $(x, -x)$ acquisition phases simply represent different sign PGSE-induced phase shifts.

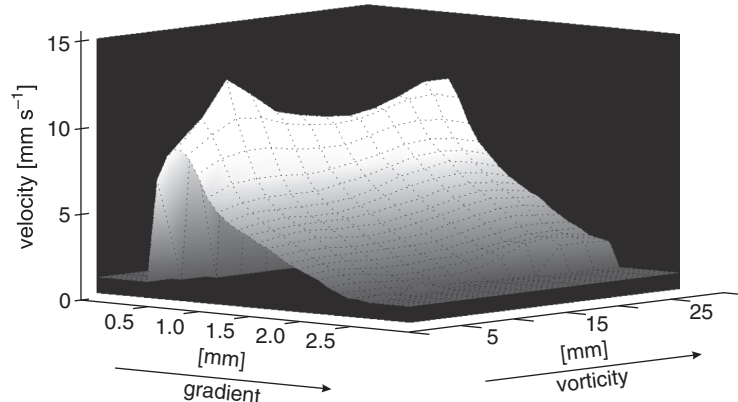


Fig. 10.11 Velocity of wormlike micellar solution under shear in the gap of a cylindrical Couette cell. The two spatial axes correspond to position across the cell gap (velocity gradient direction) and position along the cell axis (vorticity direction). (With permission from Kirk Feindel—see reference [26].)

Of course this phase cycling costs additional time, doubling the number of $q \neq 0$ encode images so that at least two RARE trains in succession are required. Given that a typical soft-pulse-quadrature-cycled PGSE-RARE train might take on the order of

500 ms, allowing for the finite duration of the 180° pulses, and the use of only every second echo, the refresh time, τ_R , is typically on the order of 1 to 2 s, T_1 recovery permitting.

An example of a 2-D velocity map taken at a refresh time of 2 s is shown in Fig. 10.11. It shows the velocity of a fluid comprising wormlike micelles being sheared in the gap of a cylindrical Couette cell, where the spatial axes correspond to the position across the cell gap (velocity gradient direction), and the position along the cell axis (vorticity direction). The image not only exhibits classic shear banding effects, in which the velocity gradient (strain rate) across the gap discontinuously changes, but also shows the degree to which the velocity profile is a function of the vorticity direction. This image is taken from one frame of a succession in which rapid fluctuations are apparent, image by image.

FLIESSEN

There is a brute force manner in which the PGSE phase shifts may be removed before each 180° RF pulse of the RARE train, thus avoiding the need to retain both the real and imaginary parts of the velocimetry phase along the entire duration of the CPMG echo train. In this variant, termed FLIESSEN, for FLow Imaging Employing a Single-Shot ENcoding [27], the PGSE gradient pulse pair is simply applied as a gradient echo of two oppositely-signed equal area pulses, within each echo cycle, and before each readout in the echo intervals, only to be unwound with an opposed pair, before the application of the next 180° pulse. The idea is simple and effective, but comes at a price of requiring that the PGSE flow observation time, Δ , be included in the echo interval for each readout, thus considerably lengthening the RARE sequence duration. The method is, however, highly suitable for rapid flows, where short Δ values are effective, and under steady-state conditions where the refresh time, τ_R , is permitted to be longer.

10.3.5 FLASH

Amongst the options which balance speed with robustness, the Fast Low Angle SHot imaging or FLASH [28] method provides a nice compromise. FLASH is based on the recall of small amounts of longitudinally stored magnetisation in a sequence of small tip-angle excitations, α_x , each of which contributes to a readout under different phase gradient positional encoding. At the penalty paid of a loss in signal-to-noise ratio due to the smaller ($\sin \alpha$) component of magnetisation tipped to the transverse plane, the method does have the advantage of a completely fresh recall at each excitation pulse, and a consequent robustness, with no contribution from recycled magnetisation contributing to image artifacts. The duration of the FLASH train is comparable with RARE, with a complete image being acquired in a few 100 ms.

Just as a precursor PGSE gradient pulse pair can be used to store flow-encoded phase in the magnetisation prior to a RARE imaging sequence, so it can be similarly applied, as shown in Fig. 10.12. Like RARE, it suffers from the fact that the PGSE-encoded phase survives as a real component only, in the case of FLASH the reason being that the flow-related phase shifts are stored in longitudinal magnetisation used for later small tip-angle recall. Of course, like RARE, it is possible to phase cycle the

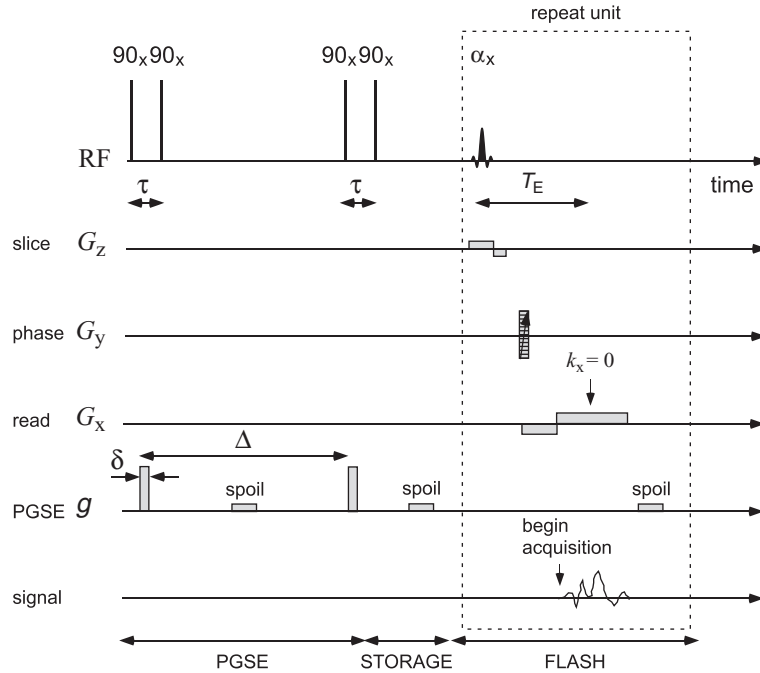


Fig. 10.12 Velocimetry pulse sequence based on FLASH using multiple small-tip-angle soft pulses, α_x , to generate each read sweep from longitudinal magnetisation that has been stored with a phase modulation due to prior PGSE-encoding for flow.

sequence so as to capture real and imaginary parts. The FLASH method has been used effectively to image xylem transport in plants [29], using a suitable phase cycle to suppress the stationary water signal.

10.3.6 SPRITE

The ultimate in imaging robustness is to be found by avoiding frequency encoding completely, so that k -space is sampled in a succession of pure phase-encoding steps. In a variant known as single point imaging [30], the spin system, initially in longitudinal Zeeman equilibrium, is subject to an applied magnetic field gradient and a broadband excitation RF pulse used to excite transverse magnetisation. Following a short time interval t_p , the NMR signal is acquired as a single point, such that the phase evolution of the spins over the period t_p provides a record of their positions under that gradient field. By repeating the process for a succession of different gradient fields, k -space is successively mapped out. The particular advantage of such single-point sampling is that all spin interactions unrelated to the changing gradient field provide a common amplitude or phase shift in the sampled signal, independent of k , and are therefore unable to contribute to image distortion. In particular, such unwanted interactions might include susceptibility-related field inhomogeneity, chemical shifts, dipolar interactions,

or spin relaxation. By making t_p sufficiently short, the effect of rapid spin–spin relaxation can be overcome, thus making single point imaging suitable for application in solids, albeit with a concomitant requirement for magnetic field gradient amplitudes sufficiently large to induce the desired phase shift over t_p .

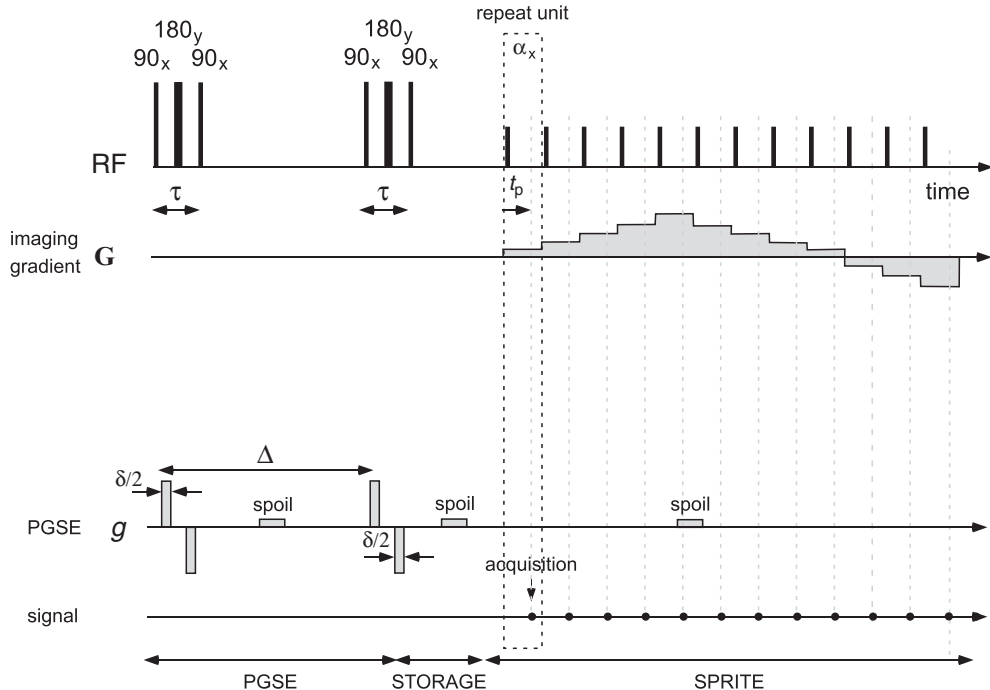


Fig. 10.13 Velocimetry pulse sequence suitable for porous media based on SPRITE using multiple small tip-angle hard pulses, α_x , to generate each single-point acquisition. A precursor 13-interval (Cotts) PGSE encoding is used to provide maximum resilience to background susceptibility related fields. The imaging part is based on a standard centric-scan SPRITE readout and the vector \mathbf{G} is successively stepped to sweep out 2-D or 3-D k -space as desired. (Adapted from Li *et al.* [31].)

Of course the method is costly in time, a feature of all pure phase-encoding methods, each step in k requiring a fresh acquisition, allowing for longitudinal relaxation recovery and gradient settling following gradient pulse switching. However, a very efficient variant, known as single-point ramped imaging with T1 enhancement, or SPRITE [32], has been proposed by Balcom *et al.* SPRITE uses a smooth transition between gradients, in a gradual ramping process, to avoid the need for gradient settling delays, and a small-tip-angle excitation pulse to allow for rapid recall of fresh transverse magnetisation. Because the method involves a very large number of phase-encoding steps (especially for two or three dimensions) a steady-state transverse magnetisation is achieved, related to the T_2^* relaxation over t_p , and the equilibrium longitudinal magnetisation associated with a sampling repeat interval T_R , tip angle α ,

and longitudinal relaxation time, T_1 [33]. Thus, the signal at each point in the image density $\rho(\mathbf{r})$ is given by the relation [32]

$$S(\mathbf{r}) = \rho(\mathbf{r}) \exp(-t_p/T_2^*) \left[\frac{1 - \exp(-T_R/T_1)}{1 - \cos \alpha \exp(-T_R/T_1)} \sin \alpha \right] \quad (10.14)$$

The use of larger than optimal turn angle⁵ has the effect of introducing a strong T_1 contrast, a useful characteristic in some applications. Because of the robustness

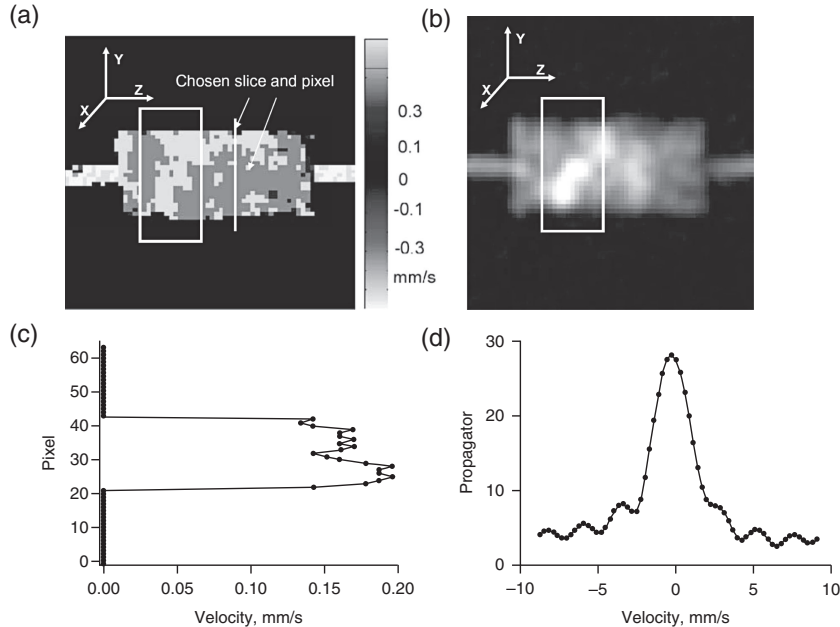


Fig. 10.14 (a) 2-D slice from the 3-D flow image in which flow is along the z -direction. A region of higher velocity, marked by the white square, indicates a high permeability channel in the rock. (b) The same 2-D slice but extracted from a 3-D T_2 -weighted image. The high intensity area, marked by the white square, indicates a high permeability channel. (c) 1-D profile of the flow map extracted from the line in (a). (d) Propagator extracted from the marked pixel in (a). (Reproduced with permission from Li *et al.* [31].)

of SPRITE, it does lend itself to challenging velocimetry imaging, for example in porous media, where strong susceptibility inhomogeneity can cause image distortion under frequency encoding, or in rapid turbulent flows where the short characteristic time interval, t_p , can be turned to significant advantage. We deal first with the porous medium case. Here the distortion-free aspect of SPRITE imaging is paramount, and the PGSE flow encoding is the standard precursor, as seen earlier in RARE or FLASH. In the present example, however, a 13-interval PGSE sequence is shown, so as to minimise the influence of background gradients due to susceptibility inhomogeneity [31].

⁵The optimum is the ‘Ernst’ angle such that $\cos \alpha_E = \exp(-T_R/T_1)$.

An example of the application of this method is shown in Fig. 10.14, where flow is imaged in a mapping of water flow through a 2.5-cm diameter, 5.24-cm-long carbonate limestone core plug coated with epoxy, at a flow rate of 2 ml min^{-1} . The core has a porosity of 27.6% and permeability of 9 mD. The experiment was carried out at 300 MHz proton frequency in a field of 7 T, giving a sample T_2^* of $500 \mu\text{s}$. Despite the short T_2^* good velocity maps are obtained and the method is able to obtain velocity distributions in a localised pixel.

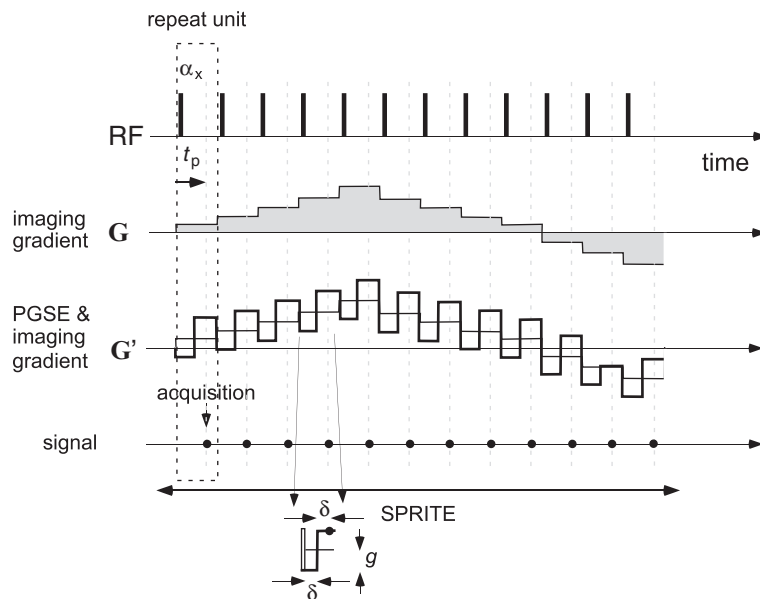


Fig. 10.15 SPRITE velocimetry pulse sequence suitable for fast flow. \mathbf{G} shows the first few gradient values of an N -point spiral trajectory, while \mathbf{G}' shows a motion-sensitised version of that trajectory. One phase-encoded data point is acquired at each circle, at a time t_p after each RF pulse. \mathbf{G}' differs from \mathbf{G} only in a symmetrical excursion ($\pm g$) either side of \mathbf{G} . Such a superposition of $\pm g$ excursions upon any k -space sampling scheme is possible. (Adapted from Newling *et al.* [34].)

Because of the large number of phase-encoding steps needed to acquire a 2-D image, SPRITE is not a fast refresh-time method, and is not well suited to the study of transient or fluctuating flows. However, it is suited to exceedingly fast flow under steady-state conditions, provided the motion-encoding time is sufficiently short. Here the inherently short characteristic sampling time of SPRITE can be turned to advantage. Figure 10.15 shows a variant of the SPRITE sequence in which the phase-encoding gradients are modulated within each sampling interval t_p , so as to provide an effective gradient echo phase encoding for spin displacement. This method has been successfully applied to the measurement of average velocity and eddy diffusivity in turbulent flow [34].

10.4 Velocimetry applications in materials science, biology, and medicine

MRI velocimetry has made a significant impact in a diverse range of fields in which complex fluid flows are significant. These include chemical engineering applications, involving catalysis and filtration, multi-phase flow in porous media, and the study of granular flow in particulate systems. In soft condensed matter physics, the method has been used to reveal deformational flow fields, both extensional and shear, as well as slip, shear banding, and flow instability. In chemical physics, MRI velocimetry has also proven useful in elucidating electro-phoretic and electro-osmotic flow, while in biological applications in-vivo flow of xylem and phloem transport in plants has been measured.

Some of these applications are briefly reviewed here. The list is intended to be illustrative rather than comprehensive.

10.4.1 Porous media flow

Amongst the advantages offered by MRI velocimetry is its inherently 3-D capacity, allowing, in principle, the measurement of the complete vector flow field. One of the more remarkable examples of such an application is shown in Fig. 10.16, where the full 3-D velocity field for water flowing in a glass bead pack has been obtained using standard 3-D spin warp with PGSE encoding for flow [35]. The selected field of view is $50.0\text{ mm} \times 50.0\text{ mm} \times 6.25\text{ mm}$, and the isotropic spatial resolution is $(195\text{ }\mu\text{m})^3$. The flow is steady-state and the total data acquisition time was 3 h. Furthermore, such 3-D flow fields obtained using MRI methods have been verified using lattice-Boltzmann simulations on identical flow geometries [36–38].

In porous media applications, it is not always necessary to encode for velocity in order to gain powerful insight. In some cases, merely obtaining a succession of MRI density images at high refresh rate can reveal subtle phenomena. This is particularly the case in two-phase (gas/liquid) flow, for example in ‘trickle-bed’ reactors, where the streamlines occupied by the fluid and gas phases may fluctuate with time, as in the hydrodynamic transition from trickle-to-pulsing flow [39]. Using a rapid FLASH MRI sequence, in which $16 \times 16 \times 32$ data arrays were acquired in 280 ms, Anadon *et al.* [40] achieved a refresh rate of 3.6 images per second, at a spatial resolution comparable with that of an individual packing element within the bed. These MRI movies are able to reveal the transition from trickle-to-pulsing flow, confirming that the transition is initiated by local pulsing events on a size-scale typical of the packing elements contained within the column [40].

Finally, it is important to remember that spatial resolution of the Eulerian flow field does not offer the only potential for powerful insight. Measurements of the distribution of velocities represented in the Lagrangian ensemble can be performed with great precision, trading away spatial encoding for a greater number of PGSE-encoding steps, allowing the generation of displacement distributions, $\bar{P}(\mathbf{R}, \Delta)$, for a range of flow times, Δ . Figure 10.17 shows an example of such propagators, for both longitudinal and transverse displacements in a bead pack, along with lattice-Boltzmann simulations. The agreement is excellent.

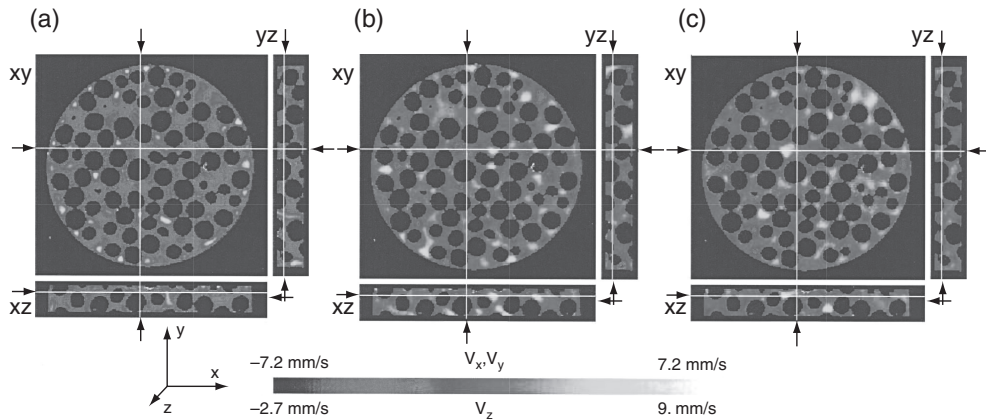


Fig. 10.16 Velocity fields within a packing of 5-mm diameter spheres within a column of internal diameter 46 mm. Fluid velocities in the (a) z -, (b) x -, and (c) y -directions are shown with slices taken in the xy , yz , and xz planes for each of the velocity components. For each image the positions at which the slices in the other two directions have been taken are highlighted. (Reproduced with permission from Sederman and Gladden [35].) This figure is reproduced in colour in the colour plate section.

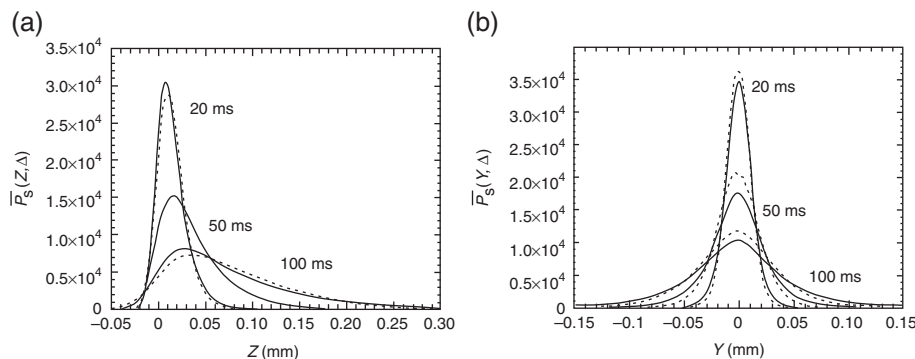


Fig. 10.17 Experimental (solid line) vs simulated (dashed line) displacement propagators along the (a) axial and (b) transverse directions for varying values of Δ for water flow in a 10-mm diameter bead pack comprising 1-mm diameter glass spheres at an average flow rate of 0.77 mm s^{-1} . (Adapted from Manz *et al.* [36].)

10.4.2 Inertial flow and turbulence

One of the more challenging uses of NMR velocimetry is in the study of inertial effects in fluid flow and the transition to turbulence. In cylindrical Couette flow at high Reynolds number, centrifugal inertial effects can lead to a complex 3-D vortex structure known as Taylor–Couette flow. The dimensionless parameter that governs this phenomenon is the so-called Taylor–Couette number [41],

$$T = \frac{2\eta^2}{1 - \eta^2} \frac{\Omega^2 d^4}{\nu^2} \quad (10.15)$$

where Ω is the inner cylinder rotation rate, ν the kinematic viscosity, d the gap width, and η the inner-to-outer radius ratio, R_i/R_o . The critical Taylor number for Taylor-Couette flow is 2510 [41], but due to the rotating bottom boundary and column aspect ratio, the onset of the instability can occur at values significantly below this. Figure 10.18 shows an example of stable 3-D velocity structure in Taylor vortices,

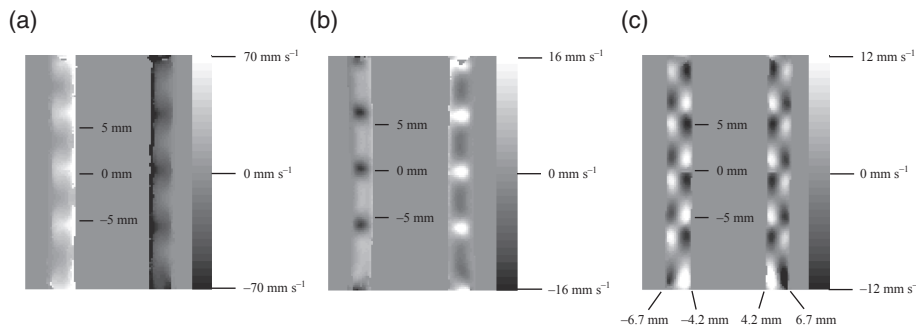


Fig. 10.18 Velocity fields for Taylor vortex motion of pentane in the gap between two concentric cylinders, at a Taylor number of 246. The cylinder is rotating such that the left-hand side is moving out of the page. (a) Radial velocity $v_r(r,z)$, (b) tangential velocity $v_\theta(r,z)$, and (c) axial velocity $v_z(r,z)$. (Reproduced with permission from Seymour *et al.* [42].)

obtained using a spin warp velocimetry sequence on pentane in a flow cell consisting of a precision-milled glass cylinder of radius $R_i = 4.2$ mm, residing in a glass tube of internal radius $R_o = 6.7$ mm, with a gap width of 2.5 mm [42]. Taylor vortex motion has also been investigated by MRI velocimetry using FLASH [43].

Applications of NMR velocimetry to turbulent flow are relatively recent [34, 44, 45], presenting significant challenges in terms of temporal resolution, but allowing for analysis of eddy diffusivity through the effective dispersion coefficient measured [34] in an experiment where PGSE gradients are stepped and a propagator analysis is undertaken.

10.4.3 Rheo-NMR

While rheology is primarily concerned with the characterisation of complex fluids and soft matter by mechanical means, flow visualisation provides a vital adjunct. In many flows there exists a need to obtain detailed information about the flow field generated by the device used to induce deformational flow, and in particular to be able to visualise, in real time, strain-rate heterogeneity and discontinuity, for example wall slip, sample fracture, and shear-banding. MRI velocimetry offers particular advantages over competing optical or ultrasound methods, both of which involve scattering from refractive index or density heterogeneity. MRI velocimetry is not subject to optical transparency constraints and, unlike these other methods, full three-dimensional velocity fields may be determined in any geometry whatsoever. The real advantage of

optical or other scattering techniques lies in their inherent speed, and hence an ability to visualise fluctuations at quite short times. However, recent advances in fast MRI velocimetry have made available refresh rates below 1 s so that many systems exhibiting transient flow behaviour have become accessible.

The idea of ‘rheo-NMR’ was first suggested by Nakatani *et al.* [46] in the context of NMR spectroscopy carried out under deformational flow. The effects of shear or extension on molecular orientation, organisation, and dynamics can potentially affect spin relaxation rates or even alter terms in the nuclear spin Hamiltonian, such as the dipolar or quadrupolar interaction. Hence, the use of MRI velocimetry to provide a map of the complex flow field represents only a part of the contribution that NMR can make to rheology. The real challenge is to be able to perform spectroscopic studies at different locations in heterogeneous flow fields, using spectroscopic MRI or spatially selective NMR spectroscopy.

In this section, we briefly traverse some examples of what is possible with rheo-NMR in the context of MRI velocimetry, noting that the subject is reviewed in greater detail elsewhere [47–50]. Furthermore, there are numerous examples involving spectroscopic applications without imaging or velocimetry, of which references [51–54] provide but a sample.

Slip and power-law flow

Figure 10.19 provides an example of how MRI velocimetry may be used to measure slip, and to characterise shear-thinning flow by power-law behaviour. The sample consists of a 46% volume fraction of 370-nm diameter core-shell latex particles suspended in a 2% (w/w) aqueous dispersion of polyvinyl alcohol [55]. The core of these particles is liquid hexadecane, making them NMR-visible. The sample has been inserted between 5-mm outer diameter (OD) inner glass cylinder and a 9.2-mm inner diameter (ID) outer cylinder and centred by two Teflon disks, this comprising the annular region of a cylindrical Couette cell. However, the same sample material also fills the inner cylinder, rotating in rigid-body motion, and thus providing a nice ‘marker’ from which the inner cylinder wall velocity may be deduced by extrapolation.

The velocity profiles, obtained at 300 MHz using a spin warp sequence, are shown for rotational frequencies $f = 8 \times 10^{-4}$ Hz, 3.2×10^{-3} Hz and 0.16 Hz, corresponding to gap-averaged shear rates $\dot{\gamma}$ of 7×10^{-3} s $^{-1}$, 0.028 s $^{-1}$ and 1.4 s $^{-1}$, respectively. At the lowest frequency, the velocity profile across the gap is completely flat and the whole sample moves like a solid plug. As the rotational frequency is increased, the shear stress across the gap increases, and in the inner regions of the gap the local shear stress exceeds the apparent yield stress σ_c of the sample, such that the outer parts of the sample at lower stress are still in the solid-like state, while the sample contained in the higher stress region near the inner wall now flows with a liquid-like, shear-thinning behaviour. Similar two-phase behaviour has been seen using MRI velocimetry in a clay and silica suspension, a concentrated oil-in-water emulsion, and a cement paste [50, 56].

For the core-shell suspension, a power-law exponent⁶ n of 0.2 can be obtained from fitting the inner part of the velocity profile to the analytical expression for the angular velocity at radius r of a power-law fluid in a wide-gap Couette geometry

⁶In the power-law model $\sigma \sim \gamma^{n+1}$.

$$v(r) = \omega r \frac{1 - (r/r_o)^{2/n}}{1 - (r_i/r_o)^{2/n}} \quad (10.16)$$

where r_i and r_o are the inner and outer radii bounding the annulus, and $\omega = 2\pi f$ is the inner-wall rotation frequency. At the highest rotational frequencies, see Fig. 10.19(c), the whole sample is liquid-like and the shear-thinning somewhat less severe, with $n \approx 0.4$.

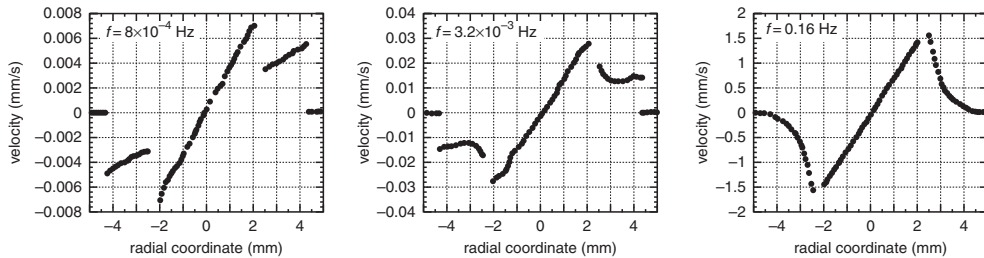


Fig. 10.19 Velocity profiles for core-shell latex particles flowing in a Couette geometry at different rotation speeds. (a) For the lowest rotational frequency $f = 8 \times 10^{-4}$ Hz, the sample behaves like a solid plug. Note the presence of slip at both the inner and at outer walls. (b) The annulus of sample near the inner cylinder, and at higher stress has undergone a solid-to-liquid transition and flows with power-law behaviour ($n = 0.2$), but the outer parts are still in a solid-like state. (c) At higher rotational speeds ($f = 0.16$ Hz), the whole sample is liquid-like and shows a power-law behaviour with $n = 0.4$. (Reproduced with permission from reference [10].)

The self-diffusion coefficient of these core-shell particles is around $10^{-13} \text{ m}^2 \text{ s}^{-1}$, corresponding to a diffusion distance of 450 nm over the PGSE encoding time of 0.5 s, around seven times the distance diffused by intra-particle molecular self-diffusion alone. Enlargement of the middle part of the velocity profile in Fig. 10.19 for the lowest rotational frequency of $f = 8 \times 10^{-4}$ Hz shows that smallest velocity measured is around 200 nm s^{-1} [10], with a displacement of 100 nm over the encoding time Δ , a factor of four smaller than the particle size. Such measurements show the potential of NMR velocimetry to measure ballistic particle collision events at very small particle velocities.

Shear banding

One of the more active areas of complex fluid research in recent years concerns the phenomenon of shear banding, in which a fluid undergoing shear flow sub-divides into two fluids of differing viscosity experiencing differing strain rates at similar stress. The effect is usually associated with the existence of a plateau in the flow curve, a phenomenon exhibited by entangled semi-dilute wormlike micelles, which undergo dissociation–recombination reactions in conjunction with reptational dynamics [57–59]. The inflected constitutive relation of Fig. 10.20(a) leads just such a plateau. In this simple picture [60], the fluid experiencing an averaged shear rate applied in the unstable (declining stress branch) region would subdivide into two coexisting ‘phases’

of high and low viscosity represented by the strain rate states $\dot{\gamma}_1$ and $\dot{\gamma}_2$, the relative proportions being determined by a simple first-order lever rule.

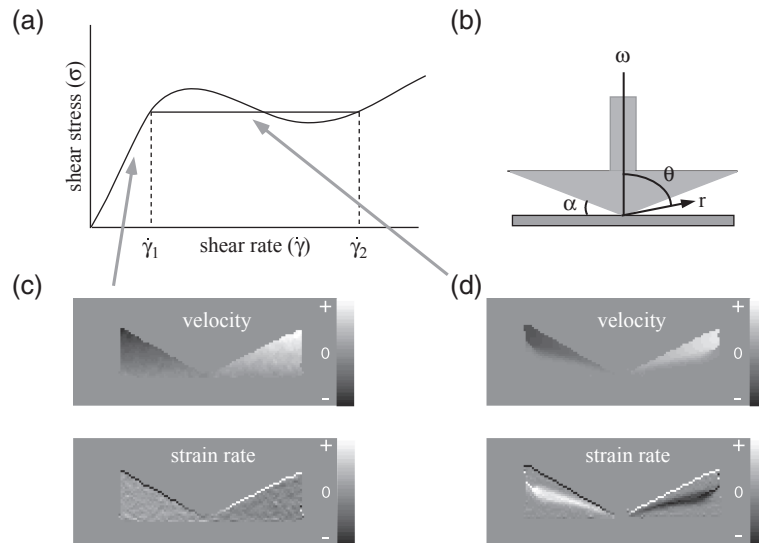


Fig. 10.20 (a) Schematic flow curve for a fluid exhibiting double-valued stress vs rate-of-strain behaviour. In the phase-separation model for shear banding, $\dot{\gamma}_1$ and $\dot{\gamma}_2$ correspond to coexisting shear rates at a single stress value. (b) Cone and plate system used in NMR microimaging experiments, showing the gap angle α . (c) and (d) show velocity and shear rate images for 100 mM/60 mM cetylpyridinium chloride/NaSal wormlike surfactant solution. The grey scales indicate the velocities and shear rates in arbitrary units. Note the opposite sign shear for the receding and advancing segments of fluid on opposite sides of the gap. (c) In a 4° gap (vertical gain $\times 6$) with free exterior fluid surface and at an apparent shear rate, $\omega/\tan\alpha$ of 1.5 s^{-1} , a uniform strain rate is apparent. (d) At 16 s^{-1} distinct shear bands are observed. (Adapted from references [61, 62].)

While optical birefringence measurements indicated the existence of banded structures in wormlike micelles [63, 64], the first direct evidence of shear-rate banding came from MRI velocimetry [61] using the wormlike micelle system 100 mM/60 mM cetylpyridinium chloride/NaSal in a cone-and-plate geometry. The device comprises a 24-mm diameter cone and plate made from the machinable glass, MACOR, with two available gap angles of 4° and 7° . Figure 10.20(c) and (d) show spin warp velocity maps, along with their derived shear rate maps, obtained from the 4° device in a 2-mm thick planar slice of spins, is excited normal to the velocity-encoding direction, such that a two-dimensional image of that plane is obtained. Note that the vertical scale is multiplied by six to provide a better visualisation of the 4° gap. At a shear rate $\omega/\tan\alpha$ of 1.5 s^{-1} , below that required to reach the stress plateau, a uniform strain-rate fluid is apparent. By contrast, at 16 s^{-1} shear banding is clearly observed. A feature of shear-banded flow is the existence of complex fluctuation dynamics, first seen in MRI velocimetry measurements [11] and shown in Fig. 10.4. These can arise from coupling

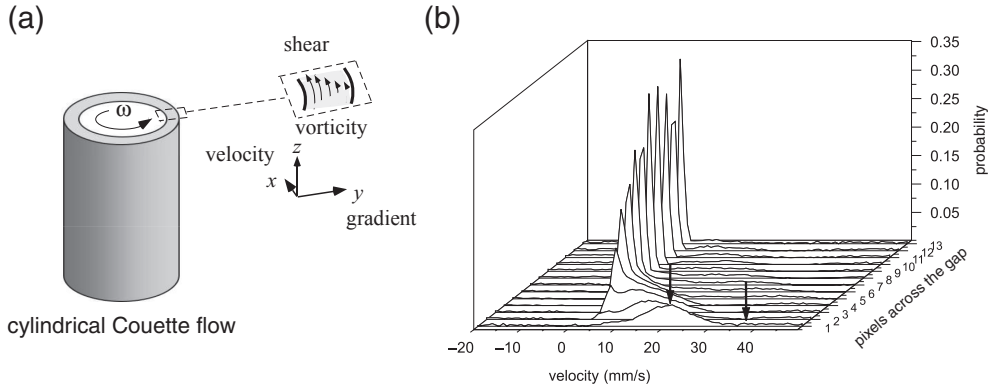


Fig. 10.21 (a) Schematic cylindrical Couette cell showing velocity, gradient, and vorticity axes. (b) Velocity distributions for the wormlike micelle system, 10% equimolar cetylpyridinium chloride/sodium salicylate in brine, in each pixel across the 1-mm gap of a 17-mm/19-mm diameter cylindrical Couette cell at a gap-averaged shear rate of 37s^{-1} . The lower velocity arrows show the positions of the mode velocities at the inner wall while the other shows the wall velocity, thus indicating slip. The broadening of distributions in the high shear band is indicative of fluctuations. (Adapted from López-González *et al.* [65].)

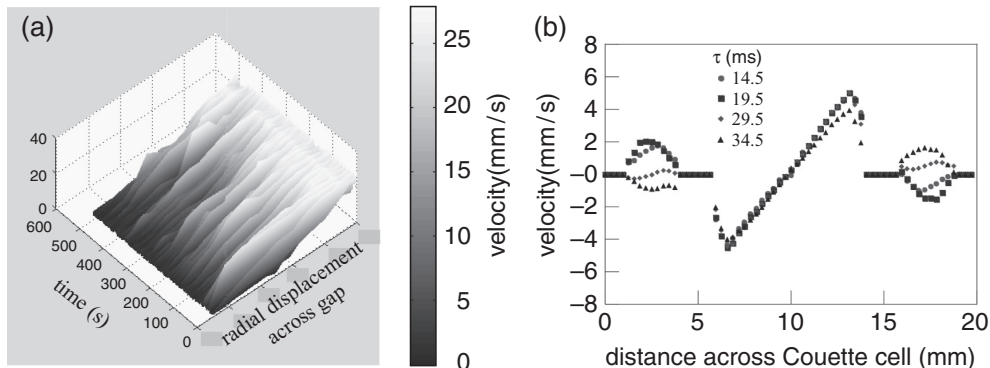


Fig. 10.22 (a) Velocity profiles for the wormlike micelle system of Fig. 10.21 across the 1-mm gap, at successive 1 s intervals, in the same 17-mm/19-mm diameter cylindrical Couette cell, also at 37s^{-1} . Here, fluctuations are directly visible. (b) Velocity profiles following the cessation of steady shear flow in a Couette cell, acquired using GERVAIS with delays of 14.5, 19.5, 29.5, and 34.5 ms. The inner cavity contains water and the outer annulus contains CPyCl/NaSal solution. (Adapted from López-González *et al.* [65] and Davis *et al.* [72].)

between flow and microstructure, as well as being the result of an intrinsic instability of planar shear-banded flow with respect to perturbations with wave vector in the plane of the banding interface [66–69], with both spatio-temporal oscillations and chaotic banded flows possible. Such fluctuations have been found in ultrasound velocimetry measurements [70] and in rapid MRI velocimetry using RARE [26, 71].

Figures 10.21 and 10.22 show two ways in which these fluctuations may be observed. In Fig. 10.21(b), spin warp MRI velocimetry, with full propagator acquisition over a 30-min experiment, reveals significantly broader velocity distributions in the vicinity of the high shear rate band, indicative of fluctuations. In Fig. 10.22(a), a single phase-encoded RARE sequence is used to obtain velocity profiles with 1 s refresh time. Here the fluctuations may be directly observed. Finally, in a most impressive demonstration of velocity image refresh speed, Fig. 10.22(b) shows the result of a cylindrical Couette cell shear-cessation experiment [72] on a wormlike micellar system using GERVAIS. Transient oscillations are seen in the wormlike micelle system occupying the annular gap, while water in the central cavity continues to rotate in the initial direction.

Molecular alignment

A fundamental driver for imaging in rheology is the role of heterogeneous deformational flow in a range of interesting rheological phenomena, including slip, shear banding, jamming and fracture, yield stress behaviour, and flow fluctuations. In consequence, a major goal for rheo-NMR is spatially resolved spectroscopic measurements. Over recent years there has been significant progress, including measuring deuterium and proton NMR line-broadening associated with shear-induced nematic order in a wormlike micelle solution, across the gap of a Couette cell [73, 74], observation of the sudden director transition that occurs in extensional flow in a four-roll mill of a magnetically aligned liquid crystalline polymer [75], and the measurement of the full alignment tensor for an entangled polymer melt [76–78]. Figure 10.23 shows elements of the alignment tensor $S_{\alpha\beta}$ for polydimethylsiloxane obtained from deuterium NMR using a 10% deuteration benzene probe molecule. The method uses selective excitation from a region of the Couette cell where the magnetic field is parallel to the relevant tensor element of interest and the resulting strain-rate-dependent tensor elements provide a powerful test of the Doi–Edwards theory [80, 81], as well as second-order variants, such as convected constraint release [82].

10.4.4 Electro-osmotic and electrophoretic flow

One potentially useful application of MRI velocimetry concerns the imaging of velocity fields in electrophoretic [83–85] or electro-osmotic flow [86, 87]. Figure 10.24 shows how a conventional spin warp velocimetry sequence can be modified to allow for the application of an electric field within the sample. Note that to avoid charge buildup effects at electrodes, such fields are generally applied with opposite sign in successive pulse cycles.

Ions undergoing electrophoretic migration collide with neutral solvent molecules, which transfer momentum in the direction of ion flow. For an ionic solution in which the charge distribution is homogeneous, the oppositely directed flow of ions and cations causes local cancellation of such effects resulting in a stationary solvent. But any inhomogeneity in charge distribution can drastically alter the local balance in electrophoretic drag forces, such that local solvent migration effects become visible, a transport phenomenon known as electro-osmosis. A nice example is provided when an ionic solution is bounded by charged surfaces, for example in a glass capillary, where the surface screening results in a separation of ions of opposite charge. Here the relocation

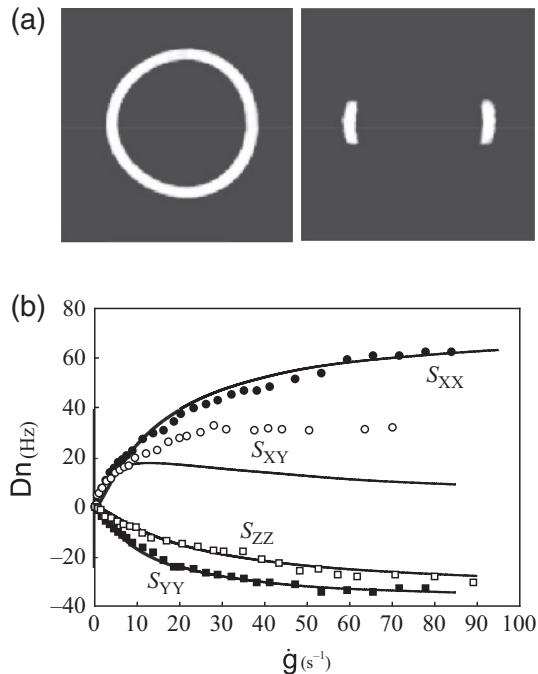


Fig. 10.23 (a) ^1H NMR images of polydimethylsiloxane polymer in the annular gap of the horizontal Couette cell, along with that obtained using a selective pulse sequence used to localise a part of the fluid. (b) Deuterium quadrupole splittings, $\Delta\nu$, as a function of shear rate obtained using localised spectroscopy from selected regions of the horizontal Couette cell in which the velocity direction (solid circles) and gradient direction (solid squares) are parallel to the magnetic field and at a 45° angle giving S_{XX} , S_{YY} , and S_{XY} (open circles), respectively. Similar measurements were done in a vertical Couette cell in which the vorticity axis is parallel to the B_0 field (open squares), giving S_{ZZ} . The solid lines are fits using Doi–Edwards theory and a polymer tube disengagement time of $\tau_d = 210$ ms. (Adapted from Cormier *et al.* [79].)

of counterions close to the surface results in an inhomogeneous distribution of mobile charges, so that application of an electric field causes inhomogeneous electrophoretic currents. An interesting consequence is that a significant slip develops within the Debye screening layer where mobile counterions predominate and fluid experiences significant drag in the direction of electrophoretic migration. Outside this layer the flow profile is determined by the hydrodynamics of a neutral fluid experiencing the electro-osmotic flow as a boundary condition [87].

Figure 10.25 shows a set of velocity images obtained for a transverse section of a water-filled 3.4-mm ID glass capillary at successively increasing values of delay time T_l using a 100 V EFP using platinum electrodes 70 mm apart. A symmetric, well-behaved velocity distribution is found below $T_l = 500$ ms, but subsequently asymmetric flow

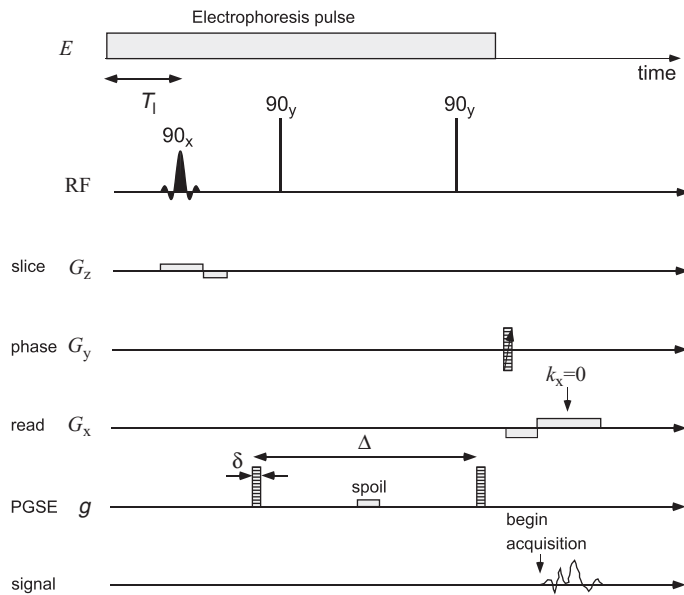


Fig. 10.24 Spin warp pulse sequence used to phase-encode the image for velocity in which an electrophoretic pulse (EFP) is included, this pulse being switched off subsequent to velocity encoding but prior to signal acquisition. Note that T_l defines the time delay between the start of the EFP and the start of the soft RF pulse. A further delay occurs before the start of velocity encoding. (Adapted from Manz *et al.* [87].)

results. The insets show a comparison of theory and experiment. Note the net zero flow in these profiles, along with the boundary slip effect [87].

10.4.5 Biology

In medical MRI, the use of velocimetry to measure blood flow is so widespread that no brief review could here suffice. Indeed, the key words ‘magnetic resonance’ and ‘angiography’ result in 11,000 references, whilst restrictions to ‘rat’ give over 100. There have been some quite spectacular uses of MRI velocimetry in plant science, including the measurement of xylem flow in a wheat grain *in vivo* [88], as well as in the xylem and phloem of castor bean *in vivo* using both spin warp [89] and FLASH velocimetry [29]. Recently MRI velocimetry has been used to measure cytoplasmic streaming velocities in single living cells, the spatial variation of the longitudinal velocity field in cross-sections of internodal cells of *Chara corallina* being imaged with a spatial resolution of 16 μm [90].

10.4.6 Granular flow

By using solid particles with liquid interior, it is also possible to use MRI velocimetry to study granular flow [91–93]. A particularly effective ‘MR-visible’ solid particle is provided by mustard seeds, and Fukushima and co-workers have used this device to

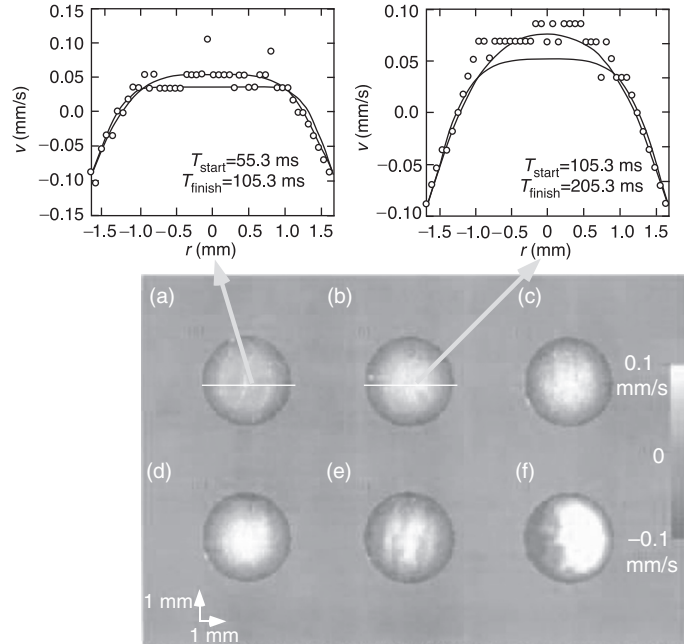


Fig. 10.25 Velocity images obtained for a transverse section of a 3.4-mm ID glass capillary at successively increasing values of delay time T_l , following application of an electric field. These delays are, respectively, (a) 50 (b) 100, (c) 200, (d) 300, (e) 500, and (f) 1000 ms. Note the asymmetric flow distribution in the image obtained at the longest time delay. Also shown are diametral profiles of velocity obtained from the images along with two theoretical profiles calculated using delay times corresponding to the start and end of velocity phase-encoding. These times are shown in the graphs for (a) $T_1 = 50$ ms and (b) $T_l = 100$ ms. (Adapted from Manz *et al.* [87].)

investigate the velocity depth profile of the flowing layer near the axial centre of a half-filled 3-D drum, confirming that it follows a quadratic form, except very close to the free surface, this deviation due to particles reaching the surface with large components of their velocity in the azimuthal direction.

Examples of their work are shown in Fig. 10.26, where in (a) a DANTE tagging sequence has been used to provide a simple flow visualisation.

10.5 Potential artifacts

Note that any use of PGSE gradient encoding is subject, in principle, to a number of systematic errors and artifacts. In particular, the measurement of self-diffusion, which relies on phase spreading, is inherently more susceptible to systematic artifacts than the measurement of velocity. This is because any effect that introduces phase incoherence will enhance the apparent diffusion rate. Such effects include sample container movement, spectrometer RF or field instability, and imperfect gradient pulse matching due to induced eddy current effects or to noise or ripple in the gradient

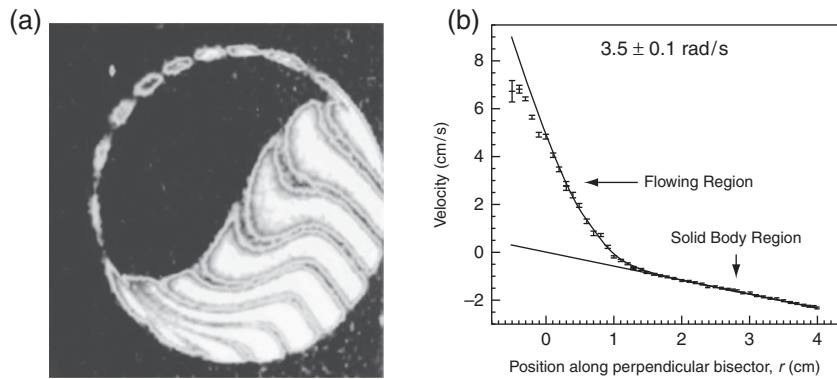


Fig. 10.26 (a) MRI tagging experiment for 2-mm diameter mustard seeds half-filling a rotating drum, in which the grains clearly separate between solid-body rotation and a flowing region. (Reproduced with permission from Nakagawa *et al.* [91].) (b) Velocity depth profiles for 2-mm mustard seeds in a half-filled cylinder along the perpendicular bisector of the free surface, averaged over five experimental runs. (Reproduced with permission from Sanfratello *et al.* [92].)

power supply. These are very standard but nonetheless troublesome problems that must be addressed by the experimenter before embarking on either standard PGSE or dynamic imaging/velocimetry experiments. Suggestions concerning counteracting these problems are given in Chapter 9 of reference [1] and Chapter 12 of this book. There are, in addition, effects peculiar to dynamic imaging and to the measurement of self-diffusion in the presence of flow, including gradient-dependent phase shifts, inflow-outflow effects, the influence of the slice selection gradient, the influence of gradient non-uniformity, and diffusion across streamlines. Again, a discussion of these is found in Chapter 8 of reference [1].

References

- [1] P. T. Callaghan. *Principles of Nuclear Magnetic Resonance Microscopy*. Oxford University Press, New York, 1991.
- [2] J. Granwehr, E. Harel, S. Han, S. Garcia, A. Pinesand, P. N. Sen, and Y-Q. Song. Time-of-flight flow imaging using NMR remote detection. *Phys. Rev. Lett.*, 95:075503, 2005.
- [3] E. Harel, J. Granwehr, J.A. Seeley, and A. Pines. Multiphase imaging of gas flow in a nanoporous material using remote-detection NMR. *Nature Materials*, 5:321, 2006.
- [4] E. Harel, C. Hilty, K. Koen, E. E. McDonnell, and A. Pines. Time-of-flight flow imaging of two-component flow inside a microfluidic chip. *Phys. Rev. Lett.*, 98:017601, 2007.
- [5] P. R. Moran. A flow velocity zeugmatographic interlace for NMR imaging in humans. *Magn. Reson. Imaging.*, 1:197, 1982.
- [6] T. W. Redpath, D. G. Norris, R. A. Jones, and J. M. S. Hutchison. A new method of NMR flow imaging. *Phys. Med. Biol.*, 29:891, 1984.

- [7] D. G. Taylor and M. C. Bushell. The spatial mapping of translational diffusion coefficients by the NMR imaging technique. *Phys. Med. Biol.*, 30:345, 1985.
- [8] P. T. Callaghan, C. D. Eccles, and Y. Xia. NMR microscopy of dynamic displacements: k-space and q-space imaging. *J. Phys. E*, 21:820, 1988.
- [9] Y. Xia. *MSc Thesis*. Massey University (unpublished), 1988.
- [10] H. Wassenius and P. T. Callaghan. Nanoscale NMR velocimetry. *J. Magn. Reson.*, 169:250, 2004.
- [11] M. M. Britton and P. T. Callaghan. Shear banding instability in wormlike micellar solutions.. *Eur. Phys. J. B*, 7:237, 1999.
- [12] P. Mansfield. Multi-planar image formation using NMR spin echoes. *J. Phys. C: Solid State Physics*, 10:L55, 1977.
- [13] P. Mansfield and I. L. Pykett. Biological and medical imaging by NMR. *J. Magn. Reson.*, 29:355, 1978.
- [14] M. Doyle, B. Chapman, R. Turner, R. J. Ordidge, M. Cawley, R. Coxon, P. Glover, R. E. Coupland, G. K. Morris, B. S. Worthington, and P. Mansfield. Real-time cardiac imaging of adults at video frame rates by magnetic resonance imaging. *Lancet*, 328:682, 1986.
- [15] R.J. Ordidge, A. Howseman, R. Coxon, R. Turner, B. Chapman, P. Glover, M. Stehling, and P. Mansfield. Microscopic imaging of slow flow and diffusion: a pulsed field gradient stimulated echo sequence combined with turbo spin echo imaging. *Mag. Reson. Med.*, 10:227, 1989.
- [16] K. Kose. Instantaneous flow-distribution measurements of the equilibrium turbulent region in a circular pipe using ultrafast NMR imaging. *Phys. Rev. A*, 44:2495, 1991.
- [17] K. Kose. One-shot velocity mapping using multiple spin-echo EPI and its application to turbulent flow. *J. Magn. Reson.*, 92:631, 1991.
- [18] K. Kose. Visualization of local shearing motion in turbulent fluids using echo-planar imaging. *J. Magn. Reson.*, 96:596, 1992.
- [19] J. C. Gatenby and J. C. Gore. Echo-planar-imaging studies of turbulent flow. *J. Magn. Reson. A*, 121:193, 1996.
- [20] A. J. Sederman, M. D. Mantle, C. Buckley, and L. F. Gladden. MRI technique for measurement of velocity vectors, acceleration, and autocorrelation functions in turbulent flow. *J. Magn. Reson.*, 166:182, 2004.
- [21] A. J. Sederman, M. D. Mantle, and L. F. Gladden. Single excitation multiple image rare (semi-rare): ultra-fast imaging of static and flowing systems. *J. Magn. Reson.*, 161:15, 2003.
- [22] T. W. J. Scheenen, D. van Dusschoten, P. A. de Jager, and H. van As. Microscopic displacement imaging with pulsed field gradient turbo spin-echo NMR. *J. Magn. Reson.*, 142:207, 2000.
- [23] T. W. J. Scheenen, F. J. Vergeldt, C. W. Windt, P. A. de Jager, and H. van As. Microscopic imaging of slow flow and diffusion: a pulsed field gradient stimulated echo sequence combined with turbo spin echo imaging. *J. Magn. Reson.*, 151:94, 2001.
- [24] P. Galvosas and P. T. Callaghan. Fast magnetic resonance imaging and velocimetry for liquids under high flow rates. *J. Magn. Reson.*, 181:119, 2006.

- [25] H. Y. Carr and E. M. Purcell. Effects of diffusion on free precession in nuclear magnetic resonance experiments. *Phys. Rev.*, 94:630, 1954.
- [26] K. W. Feindel and P. T. Callaghan. Anomalous shear banding: multidimensional dynamics under fluctuating slip conditions. *Rheo. Acta.*, 49:1003, 2010.
- [27] A. Amar, F. Casanova, and B. Bluemich. Rapid multiphase flow dynamics mapped by single-shot MRI velocimetry. *Chem. Phys. Chem.*, 11:2630, 2010.
- [28] A. Haase, J. Frahm, D. Matthei, and K. D. Merbold. FLASH imaging: rapid NMR imaging using low flip angle pulses,. *J. Magn. Reson.*, 67:258, 1986.
- [29] M. Rokitta, U. Zimmermann, and A. Haase. Fast NMR flow measurements in plants using flash imaging. *J. Magn. Reson.*, 137:29, 1999.
- [30] S. Emid and J. H. N. Creyghton. High resolution NMR imaging in solids. *Physica B*, 128:81, 1985.
- [31] L. Li, Q. Chen, A. E. Marble, L. Romero-Zerón, B. Newling, and B. J. Balcom. Flow imaging of fluids in porous media by magnetization prepared centric-scan SPRITE. *J. Magn. Reson.*, 197:1, 2009.
- [32] B. J. Balcom, R. P. Macgregor, S. D. Beyea, D. P. Green, R. L. Armstrong, and T. W. Bremner. Single-point ramped imaging with T_1 enhancement (SPRITE). *J. Magn. Reson. A*, 123:131, 1996.
- [33] R. R. Ernst, G. Bodenhausen, and A. Wokaun. *Principles of Nuclear Magnetic Resonance in One and Two Dimensions*. Clarendon Press, Oxford, 1987.
- [34] B. Newling, C. C. Poirier, Y. Zhi, J. A. Rioux, A. J. Coristine, D. Roach, and B. J. Balcom. Velocity imaging of highly turbulent gas flow. *Phys. Rev. Lett.*, 93:154503–1, 2004.
- [35] A. J. Sederman and L. F. Gladden. Magnetic resonance visualisation of single- and two-phase flow in porous media. *Magnetic Resonance Imaging*, 19:339, 2001.
- [36] B. Manz, L. F. Gladden, and P. B. Warren. Flow and dispersion in porous media: Lattice-Boltzmann and NMR studies. *AICHE J.*, 45:1845, 1999.
- [37] M. D. Mantle, B. Bijeljic, A. J. Sederman, and L. F. Gladden. MRI velocimetry and Lattice-Boltzmann simulations of viscous flow of a Newtonian liquid through a dual porosity fibre array. *Magnetic Resonance Imaging*, 19:527, 2001.
- [38] M. D. Mantle, A. J. Sederman, and L. F. Gladden. Single- and two-phase flow in fixed-bed reactors: MRI flow visualisation and Lattice-Boltzmann simulations. *Chemical Engineering Science*, 58:523, 2001.
- [39] I. Iliuta, A. Ortiz-Arroyo, F. Larachi, B. P. A. Grandjean, and G. Wild. Hydrodynamics and mass transfer in trickle-bed reactors: an overview. *Chemical Engineering Science*, 54:5329, 2001.
- [40] L. D. Anadon, A. J. Sederman, and L. F. Gladden. Mechanism of the trickle-to-pulse flow transition in fixed-bed reactors. *AICHE J.*, 52:1522, 2006.
- [41] E. L. Koschmeider. *Bénard Cells and Taylor Vortices*. Cambridge University Press, Cambridge, 1993.
- [42] J. D. Seymour, B. Manz, and P. T. Callaghan. Pulsed gradient spin echo nuclear magnetic resonance measurements of hydrodynamic instabilities with coherent structure: Taylor vortices. *Phys. Fluids*, 11:1104, 1999.
- [43] K. W. Mosera, G. Raguin, A. Harris, D. Morris, J. Georgiadis, M. Shannon, and M. Philpott. Visualization of taylor-couette and spiral poiseuille flows using a

- snapshot flash spatial tagging sequence. *Magnetic Resonance Imaging*, 18:199, 2000.
- [44] M. Sankey, Y. Yang, L. F. Gladden, M. L. Johns, D. Lister, and B. Newling. SPRITE MRI of bubbly flow in a horizontal pipe. *J. Magn. Reson.*, 199:126, 2009.
 - [45] L. Saetran C.J. Elkins, M.T. Alley and J.K. Eaton. Three-dimensional magnetic resonance velocimetry measurements of turbulence quantities in complex flow. *Experiments in Fluids*, 46:285, 2009.
 - [46] A. I. Nakatani, M. D. Poliks, and E. T. Samulski. NMR investigation of chain deformation in sheared polymer fluids. *Macromolecules*, 23:2686, 1990.
 - [47] P. T. Callaghan. Rheo-NMR: nuclear magnetic resonance and the rheology of complex fluids. *Rep. Prog. Phys.*, 62:599, 1999.
 - [48] P. T. Callaghan. Rheo-NMR and velocity imaging. *Current Opinion in Colloid and Interface Science*, 11:13, 2006.
 - [49] P. T. Callaghan. Rheo NMR and shear banding. *Rheol. Acta*, 47:243, 2008.
 - [50] P. Coussot, L. Tocquer, C. Lanos, and G. Ovarlez. Macroscopic vs. local rheology of yield stress fluids. *J. Non Newton. Fluid Mech.*, 158:85, 2009.
 - [51] A. Veron, A. E. Gomes, C. R. Leal, J. Van der Klink, and A. F. Martins. NMR study of flow and viscoelastic properties of PBLG/m-cresol lyotropic liquid crystal. *Mol. Cryst. Liquid. Cryst.*, 331:499, 1999.
 - [52] H. Siebert, P. Becker, I. Quijada-Garrido, D. A. Grabowski, and C. Schmidt. In-situ deuteron NMR investigations of sheared liquid crystalline polymers. *Solid State NMR*, 22:311, 2002.
 - [53] L. A. Madsen, T. J. Dingemans, M. Nakata, and E. T. Samulski. Thermotropic biaxial nematic liquid crystals. *Phys. Rev. Lett.*, 92:145505, 2004.
 - [54] P. Becker, H. Siebert, L. Noirez, and C. Schmidt. Shear-induced order in nematic polymer. *Macromolecules*, 220:111, 2005.
 - [55] H. Wassénius and P.T. Callaghan. NMR velocimetry and the steady-shear rheology of a concentrated hard-sphere colloidal system. *Eur. Phys. J. E.*, 18:69, 2005.
 - [56] P. Coussot, J. S. Raynaud, F. Bertrand, P. Moucheront, J. P. Guilbaud, H. T. Huynh, S. Jarny, and D. Lesueur. Coexistence of liquid and solid phases in flowing soft-glassy materials. *Phys. Rev. Lett.*, 88:218301, 2002.
 - [57] M. E. Cates. Nonlinear viscoelasticity of wormlike micelles (and other reversibly breakable polymers). *J. Phys. Chem.*, 94:371, 1990.
 - [58] N. A. Spenley, M. E. Cates, and T. C. B. McLeish. Nonlinear rheology of wormlike micelles. *Phys. Rev. Lett.*, 71:939, 1993.
 - [59] N. A. Spenley, X. F. Yuan, and M. E. Cates. Nonmonotonic constitutive laws and the formation of shear-banded flows. *J. Phys. II (France)*, 6:551, 1996.
 - [60] M. E. Cates, G. Marrucci, and T. C. B. McLeish. The rheology of entangled polymers at very high shear rates. *Europhys. Lett.*, 21:451, 1993.
 - [61] M. M. Britton and P. T. Callaghan. Two-phase shear band structures at uniform stress. *Phys. Rev. Lett.*, 78:4930, 1997.
 - [62] M. M. Britton and P. T. Callaghan. NMR visualisation of anomalous flow in cone-and-plate rheometry. *J. Rheol.*, 41:1365, 1997.

- [63] J. P. Decruppe, R. Cressel, R. Makhloufi, and E. Cappelaere. Flow birefringence experiments showing a shear banding structure in a ctab solution. *Colloid and Polym. Sci.*, 275:346, 1995.
- [64] J-F. Berret, D. C. Roux, and G. Porte. Isotropic-to-nematic transition in wormlike micelles under shear. *J. Phys. II (France)*, 4:1261, 1994.
- [65] M.R. López-González, W. M. Holmes, and P. T. Callaghan. Rheo-NMR phenomena of wormlike micelles. *Soft Matter*, 2:855, 2006.
- [66] S. M. Fielding and P. D. Omsted. Spatiotemporal oscillations and rheochaos in a simple model of shear banding. *Phys. Rev. Lett.*, 92:084502, 2004.
- [67] S. M. Fielding and P. D. Omsted. Nonlinear dynamics of an interface between shear bands. *Phys. Rev. Lett.*, 96:104502, 2006.
- [68] S. M. Fielding. Complex dynamics of shear banded flows. *Soft Matter*, 2:1262, 2007.
- [69] S. M. Fielding and H. J. Wilson. Shear banding and interfacial instability in planar poiseuille flow. *Journal of Non-Newtonian Fluid Mechanics*, 165:196, 2010.
- [70] S. Manneville, L. Becu, and A. Colin. High-frequency ultrasonic speckle velocimetry in sheared complex fluids. *Eur. Phys. J. Appl. Phys.*, 28:361, 2004.
- [71] M. R. López-González, P. Photinos, W. M. Holmes, and P. T. Callaghan. Fluctuations and order for wormlike micelles under shear. *Phys. Rev. Lett.*, 93:268302, 2004.
- [72] C. J. Davies, A. J. Sederman, C. J. Pipe, G. H. McKinley, L. F. Gladden, and M. L. Johns. Rapid measurement of transient velocity evolution using GERVAIS. *J. Magn. Reson.*, 202:93, 2010.
- [73] E. Fischer and P. T. Callaghan. Shear banding and the isotropic to nematic transition in wormlike micelles. *Phys. Rev. E*, 6401:1501, 2001.
- [74] W. M. Holmes, M. R. López-González, and P. T. Callaghan. Shear-induced constraint to amphiphile chain dynamics in wormlike micelles. *Europhys. Lett.*, 66:132, 2004.
- [75] R. J. Cormier, C. Schmidt, and P. T. Callaghan. Director reorientation of a side-chain liquid crystalline polymer under extensional flow. *J. Rheol.*, 48:881, 2004.
- [76] M. L. Kilfoil and P. T. Callaghan. Selective storage of magnetization in strongly relaxing spin systems. *Journal of Magnetic Resonance B*, 150:110, 2001.
- [77] M. L. Kilfoil and P. T. Callaghan. NMR measurement of the alignment tensor for a polymer melt under strong shearing flow. *Macromolecules*, 33:6828, 2000.
- [78] R. J. Cormier and P. T. Callaghan. Molecular weight dependence of segmental alignment in a sheared polymer melt: A deuterium NMR investigation. *J. Chem. Phys.*, 116:10020, 2002.
- [79] R. J. Cormier, M. L. Kilfoil, and P. T. Callaghan. Bi-axial deformation of a polymer under shear: NMR test of Doi-Edwards model with convected constraint release. *Physical Review E*, 6405:1809, 2001.
- [80] M. Doi and S.F. Edwards. Dynamics of concentrated polymer solutions-ii: molecular motion under flow. *J. Chem. Soc., Faraday Trans. 2.*, 74:1802, 1978.
- [81] M. Doi and S.F. Edwards. *The Theory of Polymer Dynamics*. Clarendon Press, Oxford, 1986.

490 Velocimetry

- [82] G. Marrucci and G. Ianniruberto. Stress tensor and stress-optical law in entangled polymers. *J. Non-Newt. Fluid Mech.*, 79:225, 1998.
- [83] S. J. Gibbs and C. S. Johnson. Pulsed field gradient NMR study of probe motion in polyacrylamide gels. *Macromolecules*, 24:6110, 1991.
- [84] P. Stilbs and I. Furó. Electrophoretic NMR. *Current Opinion in Colloid and Interface Science*, 11:3, 2006.
- [85] E. Pettersson, I I. Furó, and P. Stilbs. On experimental aspects of electrophoretic NMR. *Concepts in Magnetic Resonance*, 22A:61, 2004.
- [86] X. F. Zhang and A. G. Webb. Magnetic resonance microimaging and numerical simulations of velocity fields inside enlarged flow cells used for coupled NMR microseparations. *Analytical Chemistry*, 77:1338, 1998.
- [87] B. Manz, P. Stilbs, B. Joensson, O. Söderman, and P. T. Callaghan. NMR imaging of the time evolution of electroosmotic flow in a capillary. *J. Phys. Chem.*, 99:11297, 1995.
- [88] C. F. Jenner, Y. Xia, C. D. Eccles, and P. T. Callaghan. Circulation of water within the wheat grain revealed by NMR micro-imaging methods. *Nature*, 336:399, 1988.
- [89] W. Koeckenberger, J. M. Pope, Y. Xia, K. R. Jeffrey, E. Komor, and P. T. Callaghan. A non-invasive measurement of phloem and xylem water flow in castor bean seedlings by NMR microimaging. *Planta*, 201:53, 1997.
- [90] J. W. van de Meent, A. J. Sederman, L. F. Gladden, and R. E. Goldstein. Measurement of cytoplasmic streaming in single plant cells by magnetic resonance velocimetry. *J. Fluid. Mech.*, 642:5, 2010.
- [91] M. Nakagawa, S. A. Altobelli, A. Caprihan, and E. Fukushima. *Powders and Grains*, chapter NMR measurement and approximate derivation of the velocity depth-profile of granular flow in a rotating, partially filled, horizontal cylinder, page 449. R.P. Behringer and J.Y. Jenkins, eds., Balkema, Rotterdam,, 1997.
- [92] L. Sanfratello, A. Caprihan, and E. Fukushima. Velocity depth profile of granular matter in a horizontal rotating drum. *Granular Matter*, 9:1, 2007.
- [93] D. Bonn, S. Rodts, M. Groenink, S. Rafai, N. Shahidzadeh-Bonn, and P. Coussot. Some applications of magnetic resonance imaging in fluid mechanics: Complex flows and complex fluids. *Ann. Rev. Fluid. Mech.*, 40:209, 2008.